DRA

Final Report Part II

AEROSPACE ENGINEERING DEPARTMENT

TEXAS A&M UNIVERSITY

FORCE AND PRESSURE MEASUREMENTS ON AN AIRFOIL OSCILLATING THROUGH STALL

A. G. Parker

Sponsored by National Aeronautics & Space Administration - Ames Research Center under Contract No. NAS2-7917.

August 1975

TEES-3018-75-01A

TEXAS ENGINEERING EXPERIMENT STATION

FORCE AND PRESSURE MEASUREMENTS ON AN AIRFOIL OSCILLATING THROUGH STALL

Abstract

Details of force, moment and pressure distributions on a two dimensional, four foot chord, NACA 0012 airfoil, oscillating in pitch through stall, in a 7 ft. x 10 ft. low speed wind tunnel are presented. Tests were run with the airfoil in a closed test section and also in a test section having four longitudinal slots in each sidewall set to provide minimum tunnel interference on the wing in steady flow. In unsteady flow, differences between the results for the closed and 2% open case are small. The dynamic stall process is not triggered by the bursting of a laminar separation bubble but rather by the separation of the turbulent boundary layer downstream of the bubble.

Nomenclature

c – Wing chord

C_M – Pitching moment coefficient about the quarter chord

C_N – Normal force coefficient

C_p – Pressure coefficient

f – Frequency of oscillation, Hz.

K – Non dimensional frequency parameter = $\frac{\omega \ c}{2 \ U}$

R_n – Reynolds number

U – Wind velocity

x – Distance in the chordwise direction measurement from the nose of the airfoil

α – Angle of attack

ω – Angular frequency

Introduction

With the continuing development of high performance helicopters, problems associated with blade stall flutter have become of increasing concern. This arises in forward flight due to the retreating blade having to operate at higher angles of attack than the advancing blade to maintain equilibrium in roll. Often these angles are above the static stall angle of the airfoil section. Because of the oscillatory nature of the angle of attack variation through each blade revolution, the stall angle is delayed to well above static stall angles and this causes the stall, when it occurs, to be much more violent than in steady flow. This phenomena is known as dynamic stall.

Despite the amount of effort that has been spent on this problem (some of which is presented in Refs. 1-8) the mechanisms and flows leading to dynamic stall are still not fully understood. For some time it was felt by several workers[1,4,8] that the stall mechanism was closely linked with the behavior of the leading edge laminar separation bubble, but recent developments[9] throw considerable doubt on this theory. It was based on a belief in the "leading edge bubble concept" that the current program of experimental work was undertaken. Because of the small size of the laminar separation bubble, tests were required using larger models which led to large tunnel interference that could not be allowed for in oscillatory testing through stall.

In steady flow, tunnel interference can be reduced significantly by the use of slotted tunnel walls[10,11]. Initial tests were therefore conducted to ascertain the best slot configuration to reduce the required corrections on a 4 ft. chord 2 dimensional NACA 0012 wing[12]. It was assumed that this self correcting of the tunnel would also be valid for unsteady tests in the range of frequencies considered.

The program was then planned to obtain detailed pressure measurements on the 4 ft. chord wing oscillating in pitch and to compare data in a closed tunnel with that obtained in a tunnel where the walls were slotted for minimun corrections. It is the results of these tests that are given here.

The report on this work is presented in two parts. The first contains all the data obtained but does not include a detailed discussion of the results. This is undertaken in the present second part where the more significant data is discussed in greater depth.

Equipment and Tests

All tests were conducted in the Texas A&M University's 7' x 10' Low Speed wind tunnel, using a two dimensional NACA 0012 airfoil spanning the short dimension of the tunnel. (Figs. 1, 2) The airfoil was pivoted at its quarter chord and could be oscillated in pitch using a variable speed electric motor.

Initial tests to measure the normal force coefficient (C_N) and the quarter chord pitching moment coefficient (C_M) required the installation of ten Validyne DP9 pressure transducers connected between the upper and lower surfaces of the wing at several chordwise locations (Table 1). Outputs from these transducers were fed through an operational amplifier summing circuit[13] (Figs. 3, 4) to give output voltages directly proportional to C_N and C_M. These outputs were then recorded on a Honeywell Visicorder along with the angle of attack (α) of the airfoil.

The solid sidewalls of the tunnel were removed and replaced with walls having four longitudinal slots the width of which could be varied. (Fig. 2) Early tests[12] indicate that tunnel corrections could be minimized with the sidewalls set for 2% open. All subsequent tests were performed for the tunnel sidewalls both closed and 2% open.

Oscillatory tests were conducted at three Reynolds numbers(R_n), 1×10^6, 2×10^6 and 3×10^6 and for four frequency parameters, $K = \frac{\omega c}{2U}$, of 0.022, 0.05, 0.065 and 0.15. In each case the angle of attack was varied sinusoidally about a mean angle of 16 degrees

with an amplitude of $\pm$ 10 degrees. Data was obtained for several cycles and for each test a "typical" cycle was chosen and the data plotted in the form of curves of C_N - α and C_M - α, Figs. 5-28.

As well as overall forces and moments, detailed pressure distribtributions were measured. To do this, ten more transducers were installed in the wing. Of the twenty transducers, twelve were connected to the upper surface and eight to the lower surface (Table 2). The reference sides of all these transducers were connected to a plenum in the wing which was held at free stream static pressure. Outputs from all the transducers were recorded individually on visicorders to give time histories of the pressure at each location (Fig. 29).

Pressure data was obtained for all the previous configurations and again results for "typical" cycles were carpet plotted in the form of the pressure coefficient, C_p, versus x/c, versus α (Figs. 30-49).

Discussion

In all the tests there was considerable variation in the recorded data from cycle to cycle due to the stall process not being quite identical each time. Averaging results over several cycles might, however, result in a loss of definition of the sharp peaks caused by vortex shedding that occurs in all cycles but at slightly different points in each cycle. For each test a "typical" cycle was therefore chosen and the data presented here.

a) $C_N \sim \alpha$

Results for the low frequency parameter (k = .022) are presented in Figs. 5-7. The angle of attack for lift stall varies from 19^o to 21.5^o for Reynolds numbers increasing from 1 to 3 million.

The sharp peak at C_N max that occurs for R_n = 1 and 2 million does not appear in the plot for R_n = 3 million because the quality of recording paper used for that test was poor and data in the region of C_N max could not be extracted (Note - this also occurred for K = 0.065).

Full recovery from the stall occurred at all Reynolds numbers when the angle of attack had decreased to about 12 degrees.

For K = 0.05 (Figs. 8-10) the angle of lift stall has increased slightly (21 to 22 degrees depending on Reynolds number) causing an increase in C_N max. Also the angle of attack for lift recovery has decreased to 10 degrees and it should be noted that the minimum value of C_N no longer occurs at the minimum angle of attack.

These trends of increasing stall angle and C_N max with increasing frequency parameter continue for K = 0.065 (Figs. 11-13) and K = 0.15 (Figs. 14-16) but at K = 0.15 the lift stall angle is the same for all

Reynolds numbers (25.4 degrees) and is very close to the maximum angle of attack reached during the cycle. C_N max has increased to 2.6 and the loss of lift after stall is very rapid. Recovery from stall does not occur until the minimum angle of attack is reached.

In the results for all frequency parameters the normal force rises rapidly and non-linearly just prior to stall. This occurs after initial boundary layer separation (see discussion on pressure distribution) and is probably due to the increasing strength of the vortex due to boundary layer separation, as it forms prior to being shed and convected downstream.

Under most test conditions there are several "spikes" in the $C_N \sim \alpha$ curve just after stall indicating the shedding of more than one vortex.

b) $C_M \sim \alpha$

For the low frequency parameter (Figs. 17-19) pitching moment stall occurs between 16 and 20 degrees angle of attack depending on Reynolds number. Until the onset of stall, C_M remains zero but then moves rapidly negative as the shed vortex moves back over the wing. Full moment recovery occurs at about 12 degrees angle of attack when C_M returns to zero.

As the frequency parameter is increased to 0.05 (Figs. 20-22) and 0.065 (Figs. 23-25), the angle of moment stall increases but is still Reynolds number dependent. At the highest K (Figs. 26-28) the angle of moment stall again increases but, as with the angle of lift, stall at this K becomes independent of Reynolds number. Stall occurs at 24° in all cases. Very large, first negative then positive,

values of $\frac{dC_M}{d\alpha}$ occur just after stall producing C_M minimums of -0.5. As with C_N at this high frequency, recovery does not occur before α minimum has been reached.

Moment stall occurs before lift stall. Increasing suction associated with the separating vortex causes large negative pitching moments whilst normal force is still increasing. Moment recovery occurs later than lift recovery.

Vortices shed from the leading edge have a much greater effect on the pitching moment than the normal force so the C_M traces are much more erratic than the C_N traces and the spikes due to shedding of subsidiary vortices more apparent.

c) $C_p \sim \alpha$

Raw data traces of the surface pressure variations (Fig. 29, $R_n = 2 \times 10^6$, K = 0.15, tunnel 2% open) show that as the upper surface pressures decrease with increasing angle of attack the laminar separation bubble moves forward. The bubble is first apparent at $\alpha = 9^o$ as it crosses the port located at x/c = 0.05 and by $\alpha = 16.5^o$ it has moved forward to port x/c = 0.0125. First indications of stall are observed at x/c = 0.05 at $\alpha = 23.5^o$ (half a degree before the onset of moment stall on the force traces) with a slight loss of suction indicating the start of boundary layer separation. As the angle of attack continues to increase the point of boundary layer separation (as indicated by minima in the pressure traces) moves rapidly forward reaching the nose at $\alpha = 24^o$.

At $\alpha = 24.1^o$ the pressure at x/c = 0.1 starts to decrease rapidly due to the vortex being formed by the boundary layer separation increasing in strength, this coincides with the onset of moment stall and the start of the rapid increase in C_N prior to lift stall (Figs. 15 and 27).

The pressure at x/c = 0.1 reaches a minimum at $\alpha = 24.7^{o}$ indicating that the vortex has been shed and is moving downstream. Successive minima at port locations aft of x/c = 0.1 confirm this and show that the vortex moves at about 45% of the free stream velocity. Smaller suction peaks after the initial minimum indicate the shedding of more than one vortex.

As the onset of boundary layer separation occurs downstream of the bubble, and subsequently propagates forward towards it, it is apparent that the bubble itself is not the primary trigger mechanism of the stall and that the turbulent boundary layer aft of the bubble separates as suggested in Ref. 9.

Reattachment occurs first near the nose when $\alpha \approx 16^{o}$-19^{o} and moves towards the trailing edge at approximately 30% of the free stream velocity reaching x/c = 0.9 when $\alpha = 8.5^{o}$. However it should be noted that whilst reattachment of the boundary layer is complete, neither C_N nor C_M recover until minimum angle of attack has been reached.

Only one case has been discussed but the data traces for other frequency parameters and Reynolds numbers are similar, differing mainly in the angle of attack at which the stall process starts.

When the pressure data is reduced and carpet plotted in the form $C_p \sim x/c \sim \alpha$ (Figs. 30-49), some of the details described above (e.g. the forward motion of the bubble prior to stall) are lost because of the scaling required. However the plots do show the build up of lift to the point of stall and the movement downstream of the suction peak due to the shed vortex after stall.

The general trends noted in the force measurements are clearly indicated i.e. increasing stall angle with increasing frequency parameters little effect of Reynolds number aside from increasing the stall angle at low frequencies and only minor differences (less than cyclic variations) between the tunnel closed and 2% open configurations.

One interesting effect is the motion of the forward stagnation point. For the case previously described ($R_n = 2 \times 10^6$, $K = 0.15$, tunnel 2% open) the stagnation point starts at $x/c = 0.0125$ on the lower surface at α minimum and moves back to about $x/c = 0.1$ just prior to the start of stall at $\alpha = 24^o$. Soon after stall it moves rapidly forward and by $\alpha = 22^o$ it is back at $x/c = 0.0125$ where it remains for the rest of the cycle. This behaviour is qualitatively the same for all the other frequencies tested.

d) Effects of Slotted Walls

In steady flow there are significant corrections required to data obtained on a 4 ft. chord 2 dimensional NACA 0012 airfoil in a 7' x 10' wind tunnel but they can be reduced considerably by a 2% opening of the tunnel sidewalls[12] In unsteady flow, at all the frequencies tested, differences in results between tunnel closed and 2% open were smaller than cyclic variations in any one test. Even the stall angles were the 'same' for the two configurations.

This indicates that in unsteady flow either the 2% opening is insufficient to minimize the corrections or that the dynamics of the flow about the wing (i.e. the build up and loss of lift) is such that it

is almost equivalent to "free air" conditions. Whilst the author cannot prove the latter it is felt that it is the more probable. The frequencies used particularly for the low values of K, were so low that the pressure fields on the tunnel walls should respond as though the flow were steady, and therefore the wall porosity required for minimum corrections should be similar to the steady flow case.

Conclusions

Increasing Reynolds number from 1×10^6 to 3×10^6 increases the angle of attack at which dynamic stall occurs. This effect decreases with increasing frequency parameter. Reynolds number does not have any effect on the nature of the stall process, the same type of stall occurs at all the Reynolds numbers tested.

Differences between results obtained in a closed tunnel and a tunnel with the sidewalls 2% open were in all cases smaller than the cyclic variations in each test. It appears that the wind tunnel corrections required for unsteady flow through stall in a closed tunnel are significantly smaller than those required for steady flow.

The dynamic stall process is not triggered by the bursting of a leading edge laminar separation bubble, rather the turbulent boundary layer downstream of the bubble separates first and the separation point moves forward to the bubble.

The vortex shed in the stall process moves downstream at about 45% of the free stream velocity. Boundary layer reattachment after the stall occurs first near the nose and moves downstream at about 30% of the free stream velocity.

Since the stall process starts with a breakdown of the turbulent boundary layer rather than the bursting of a bubble it might be possible, at least for the two dimensional case, to develop a theoretical model that will predict the stall characteristics. Any such theoretical approach should however allow for the motion of the front stagnation point.

References

1. Ham, N. D. and Garelick, M. S. "Dynamic Stall Consideration in Helicopter Rotors" Journal of the American Helicopter Society, Vol. 13 April 1968, pp. 49-55.

2. Parker, A. G. and Bicknell, J. "Some Measurements on Dynamic Stall" AIAA Journal of Aircraft, Vol. 11, No. 7 July 1974 pp. 371-374.

3. Martin, J. M., Empey, R. W., McCroskey, W. J. and Caradonna, F. X. "An Experimental Analysis of Dynamic Stall on Oscillating Airfoil" Journal of the American Helicopter Society, Vol. 19, No. 1 Jan. 1974 pp. 26-32.

4. Silcox, R. J. and Szwarc, W. J., "Wind Tunnel Dynamic Analysis of an Oscillating Airfoil", AIAA Paper No. 74-259, Washington, D. C. Jan 1974.

5. Carta, F. O. "Chordwise Propagation of Dynamic Stall Cells on an Oscillating Airfoil" AIAA Paper No. 75-25, Pasadena, California Jan. 1975.

6. Ericsson, L. E. and Reding, J. P. "Dynamic Stall Analysis in the Light of Recent Numerical and Experimental Results." AIAA Paper No. 75-26 Pasadena, California Jan. 1975.

7. Johnson, W. and Ham, N. D. "On the Mechanism of Dynamic Stall" Journal of the American Helicopter Society, Vol. 17 No. 4 Oct. 1972 pp. 36-45.

8. McCroskey, W. J. and Fisher, R. K. Jr., "Detailed Aerodynamic Measurements on a Model Rotor in the Blade Stall Regime" Journal of the American Helicopter Society, Vol. 17 No. 1 Jan. 1972, pp. 20-30.

9. McCroskey, W. J., Carr, L. W. and McAllister, K. W. "Dynamic Stall Experiments on Oscillating Airfoils" AIAA Paper No. 75-125, Pasadena, California January 1975.

10. Pearcey, H. H., Sinnot, C. S. and Osborne, J. "Some Effects of Wind Tunnel Interference Observed in Tests on Two-Dimensional Aerofoils at High Subsonic and Transonic Speeds" AGARD Report 296 March 1959.

11. Parkinson, G. V. and Lim, A. K. "On the Use of Slotted Walls in Two-Dimensional Testing of Low Speed Airfoils" C.A.S.I. Transactions Vol. 4, No. 2 Sept. 1971.

12. Parker, A. G. "Use of Slotted Walls to Reduce Wind-tunnel Boundary Corrections in Subsonic Flow" AIAA Journal, Vol. 12 No. 12 Dec. 1974, pp. 1771-1772.

13. Private communication between A. G. Parker and K. W. McAllister.

Table I

Transducer Locations For Force Measurements

Transducer No.	Transducer Location $(\frac{x}{c})$
1	.025
2	.05
3	.10
4	.15
5	.20
6	.30
7	.40
8	.60
9	.70
10	.90

All transducers connected between the upper and lower surfaces.

Table II

Transducer Locations For Pressure Measurements

Transducer No.	Transducer Location $(\frac{x}{c})$	
1	0	Upper Surface
2	0.001	
3	0.005	
4	0.0125	
5	0.025	
6	0.05	
7	0.1	
8	0.2	
9	0.3	
10	0.4	
11	0.6	
12	0.9	
13	0.001	Lower Surface
14	0.0125	
15	0.1	
16	0.2	
17	0.3	
18	0.4	
19	0.6	
20	0.9	

All transducers referenced to tunnel static

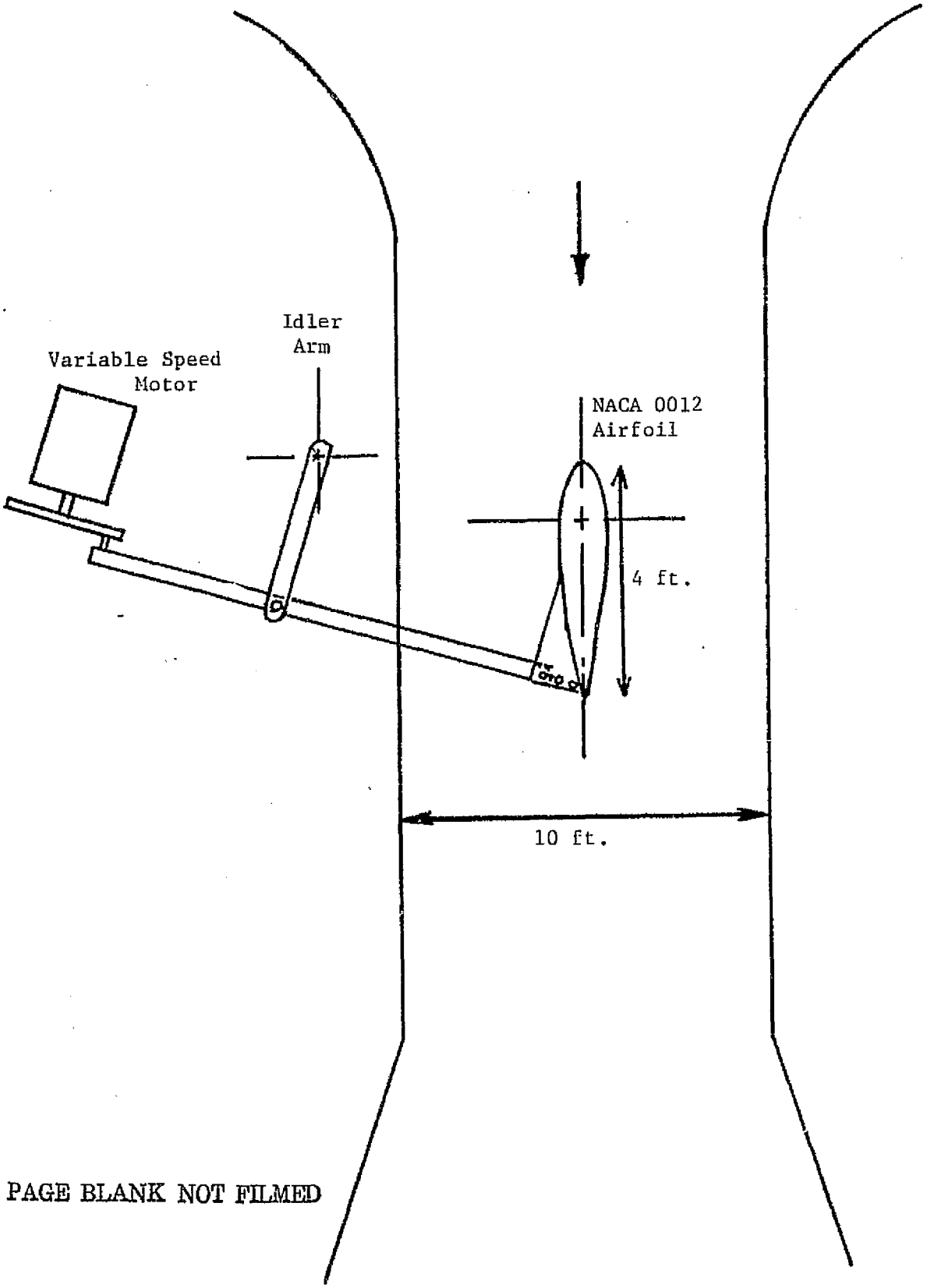

PRECEDING PAGE BLANK NOT FILMED

Fig. 1: Schematic of Test Equipment

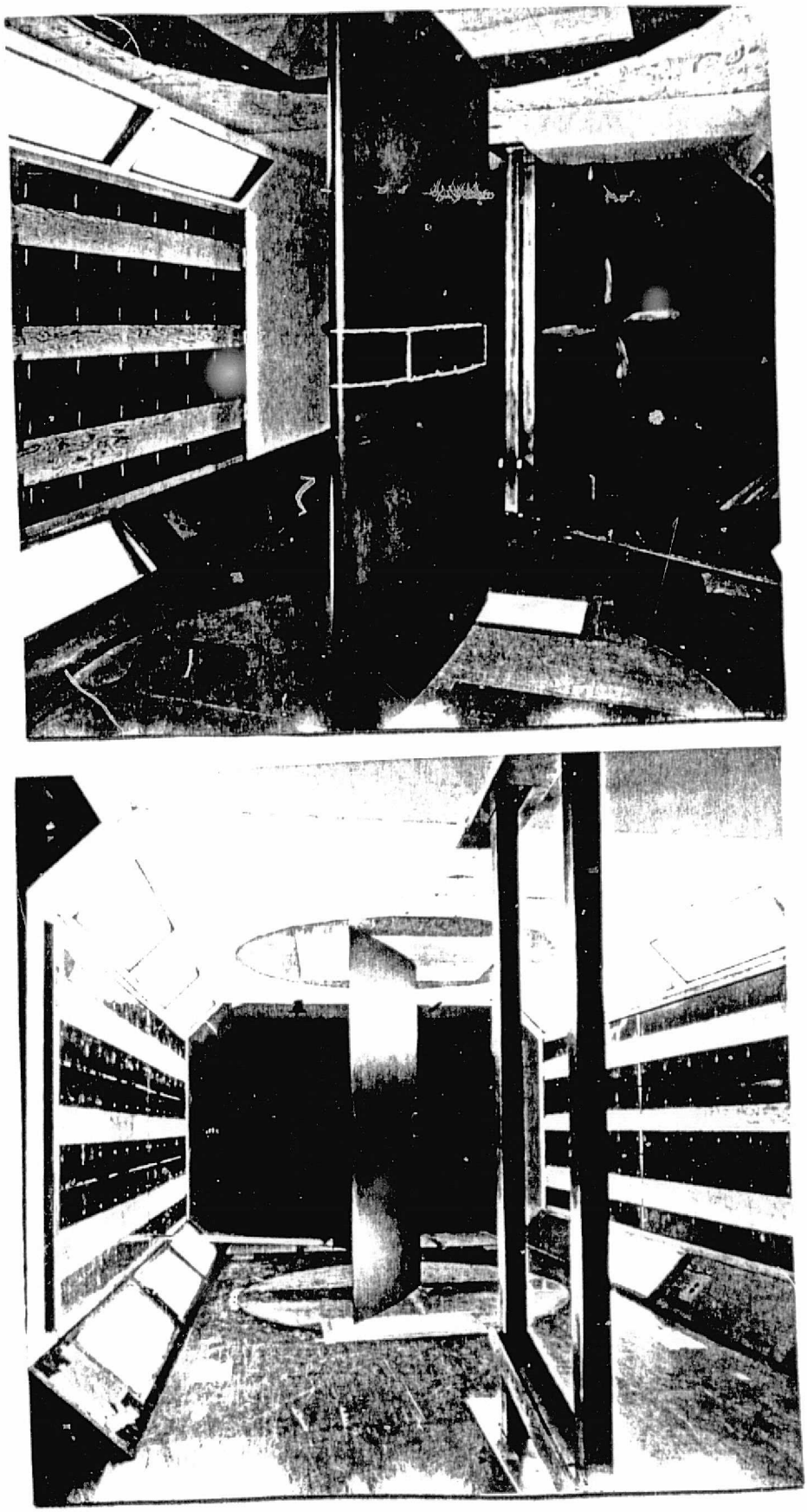

Fig. 2 Details of Test Equipment

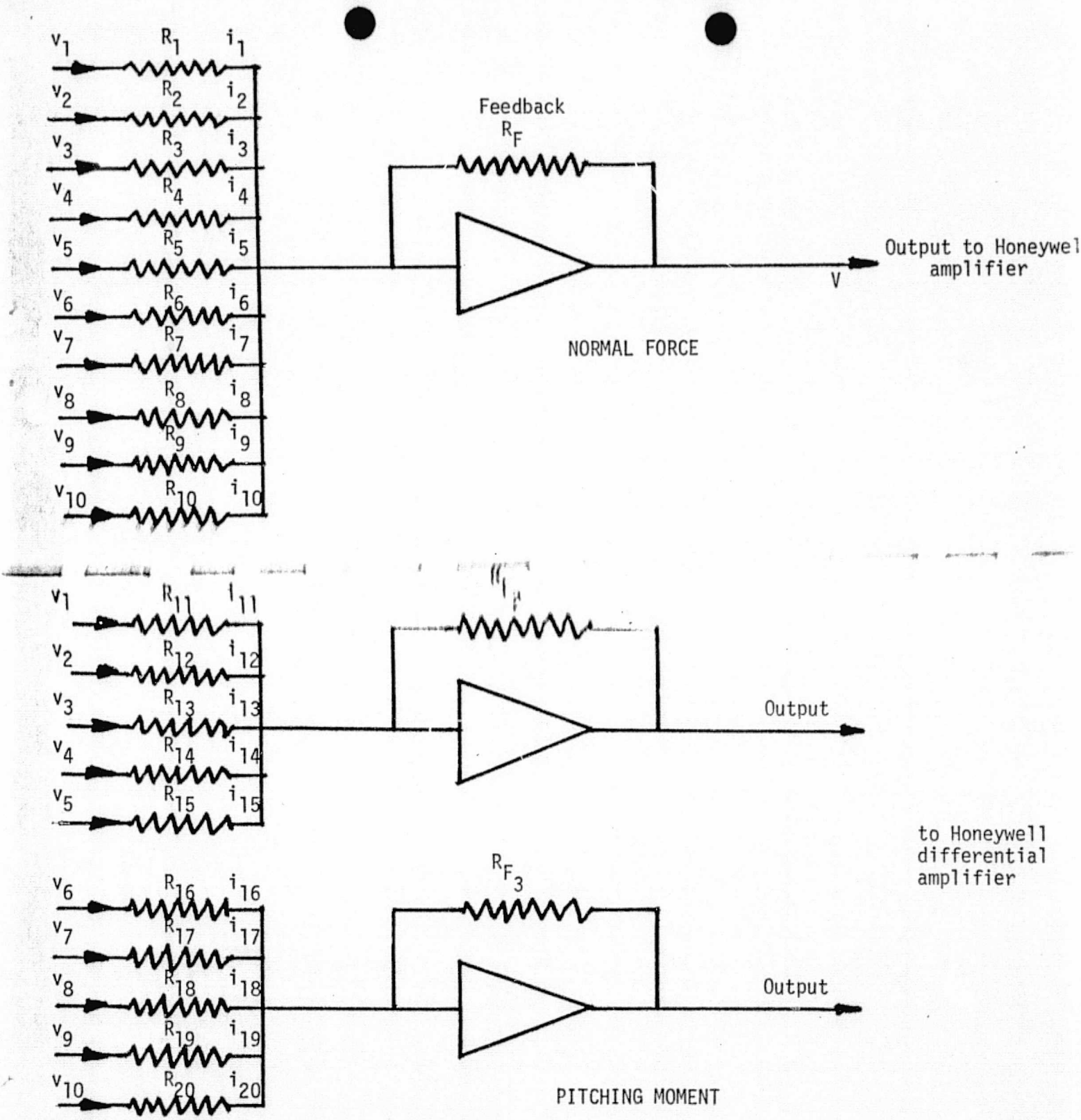

Fig. 3 Electronic Summers

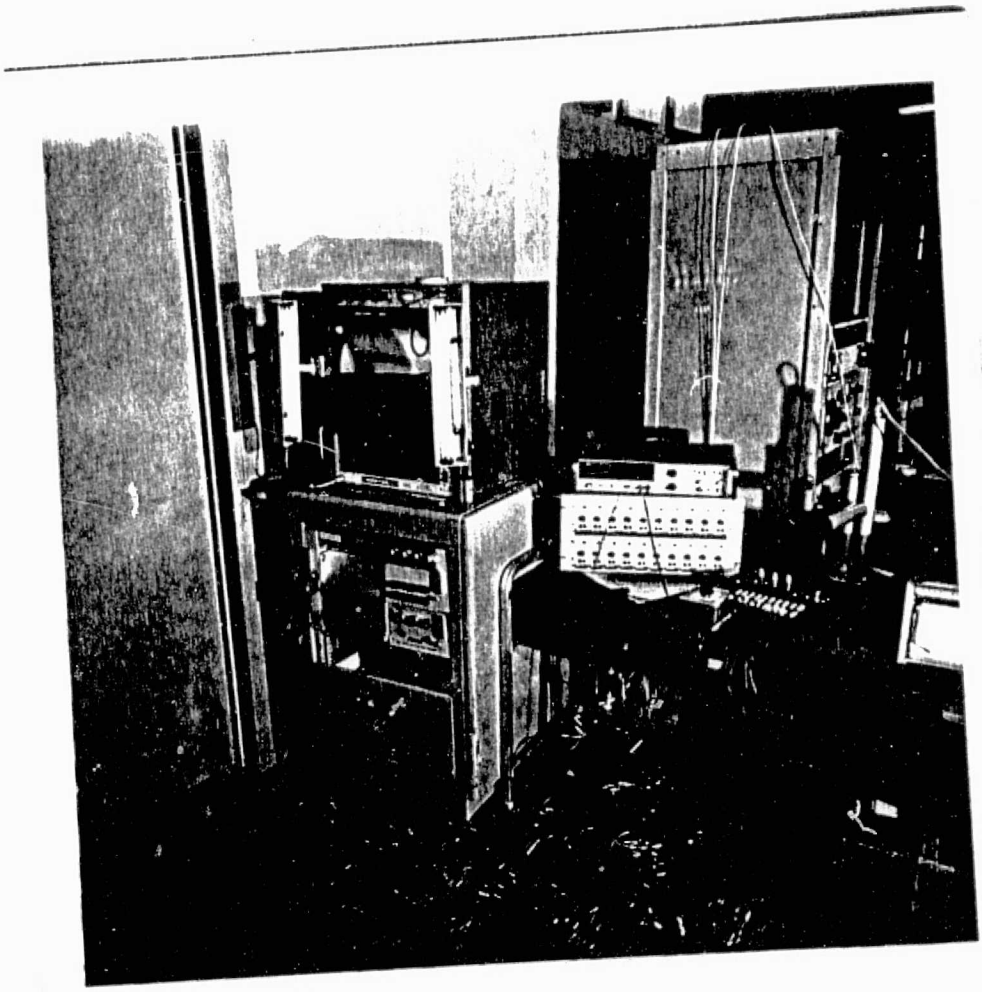

Fig. 4 Test Instrumentation

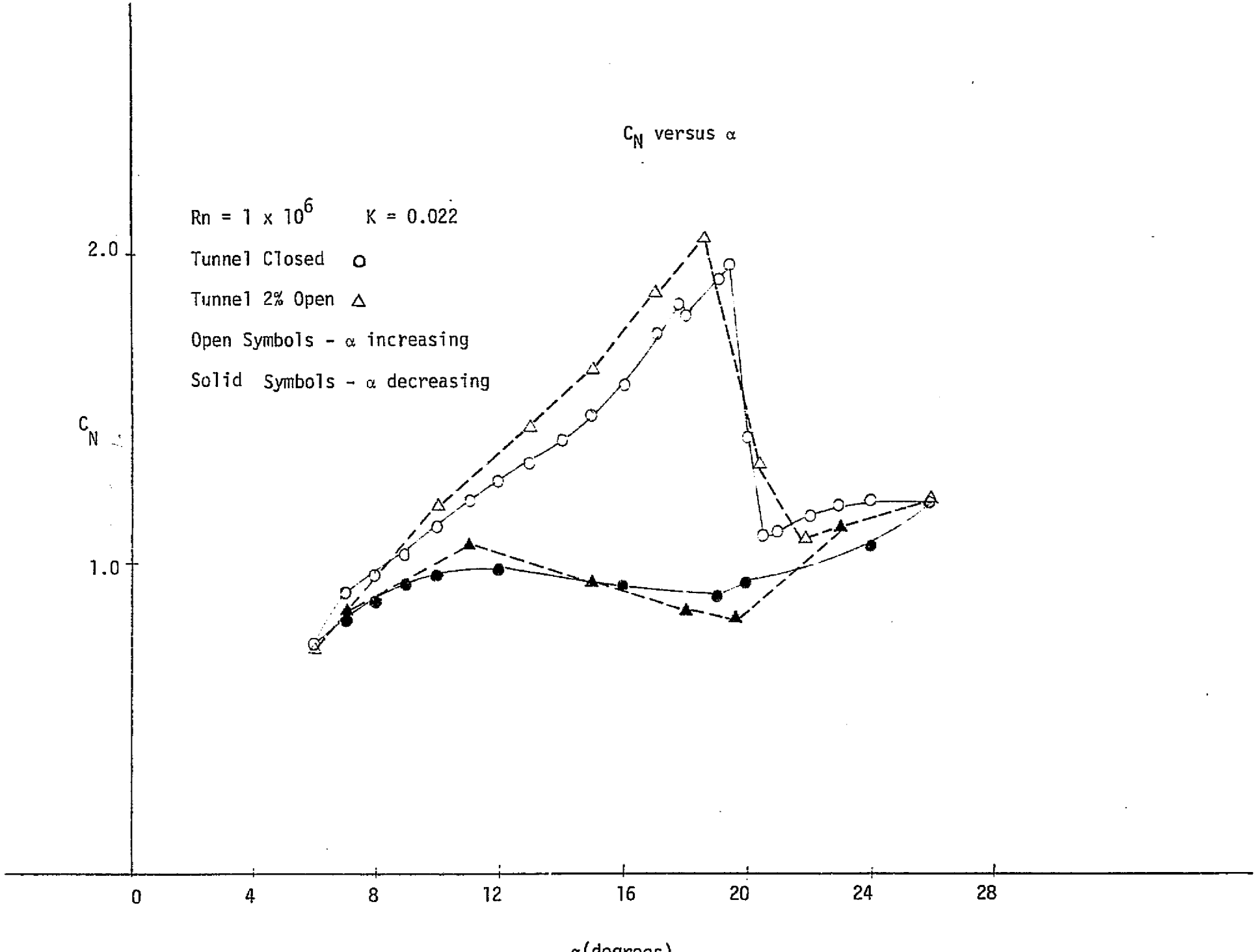

Fig. 5: C_N versus α, R_n = 1x10^6, K = 0.022

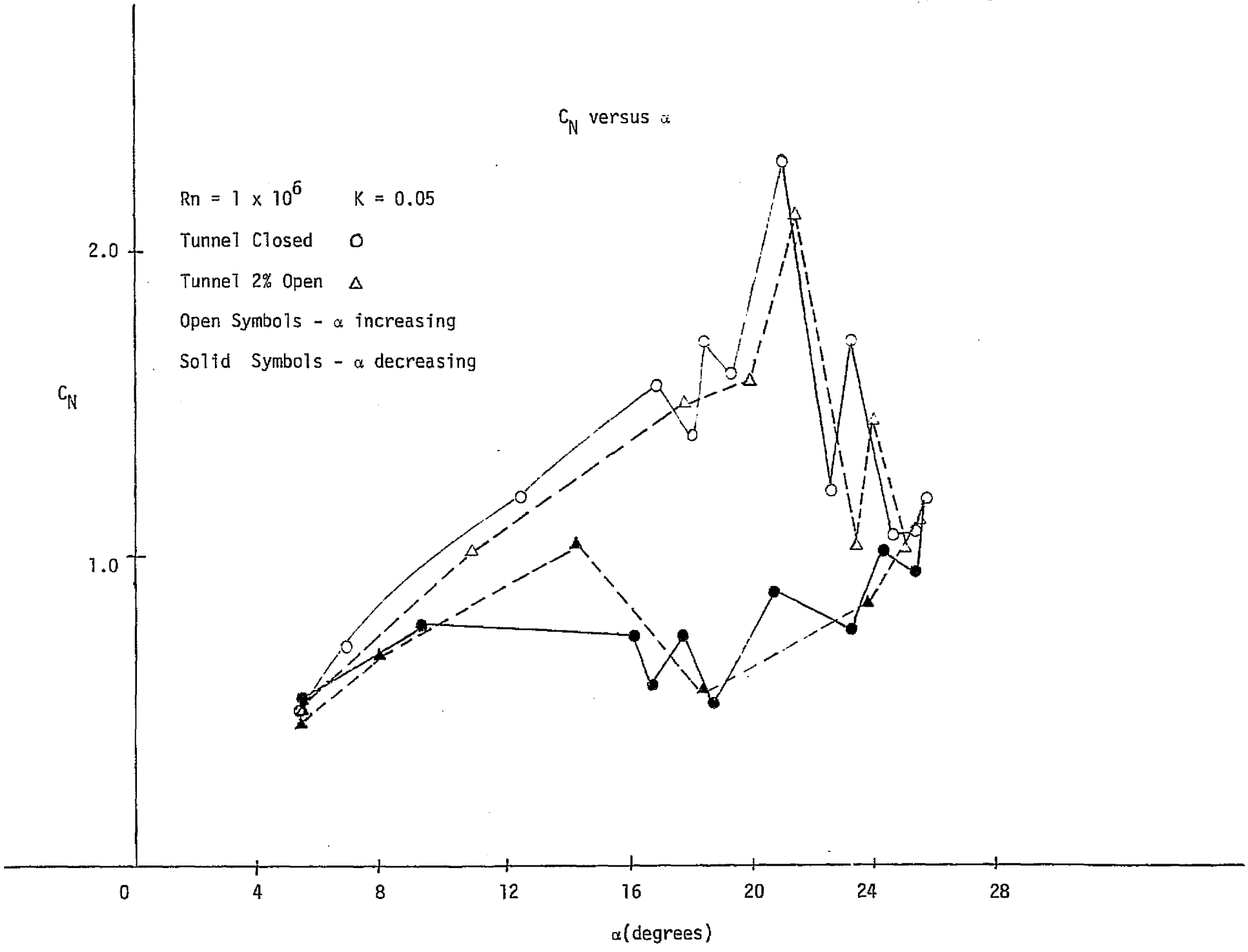

Fig. 6: C_N Versus α, R_n = 1 x 10^6, K = 0.05

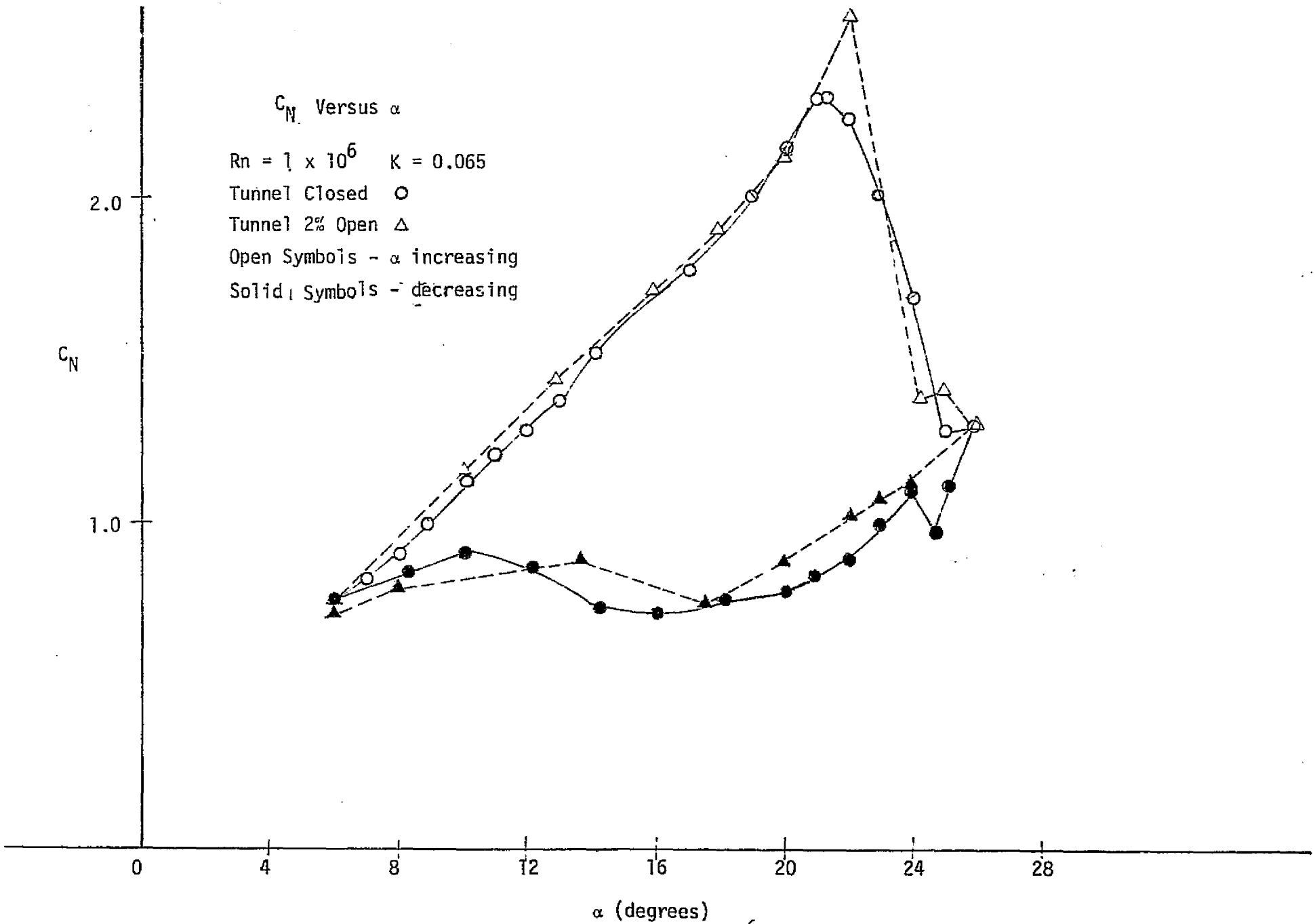

Fig. 7: C_N versus α, R_n = 1 x 10^6, K = 0.065

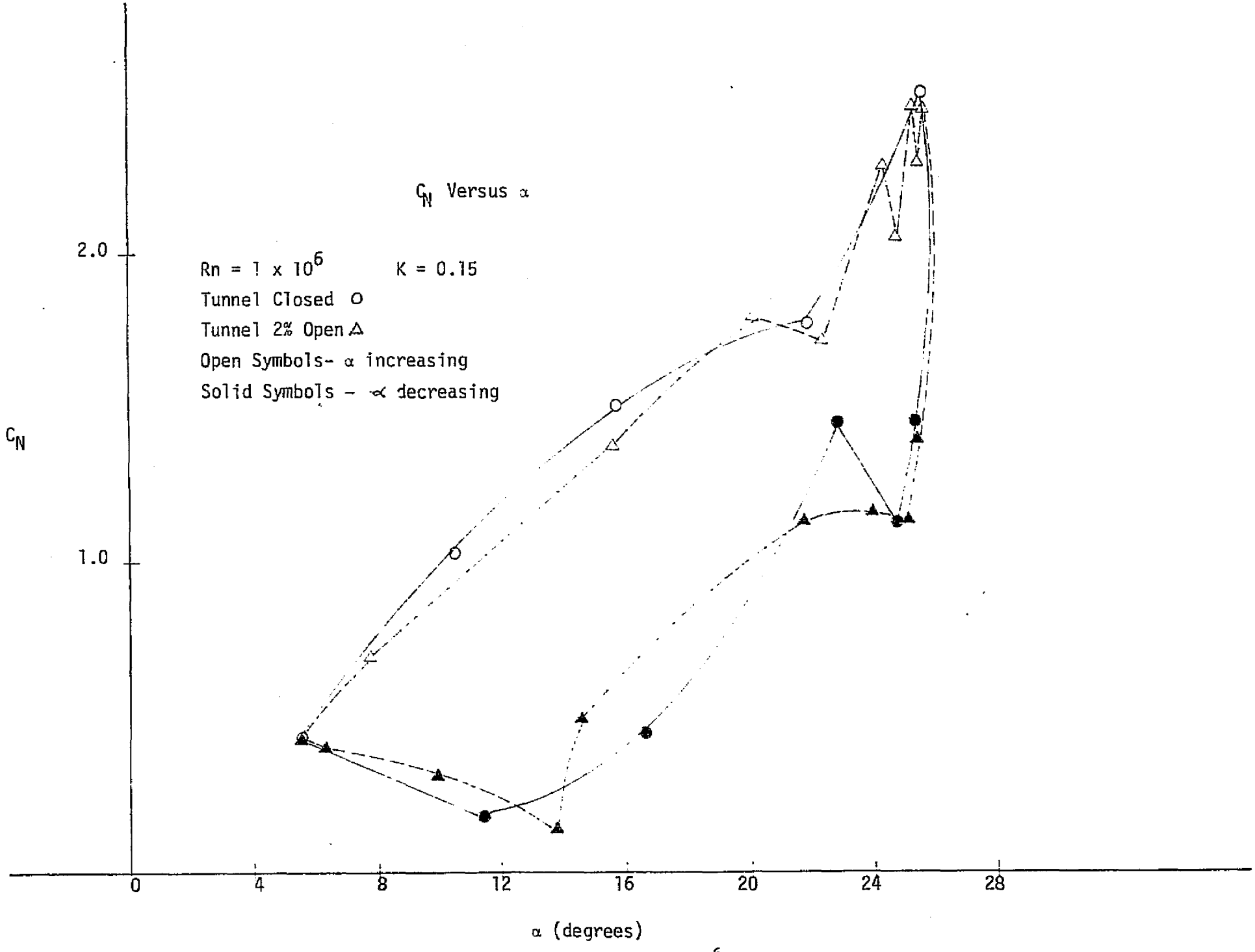

Fig. 8: C_N Versus α, R_n = 1 x 10^6, K = 0.15

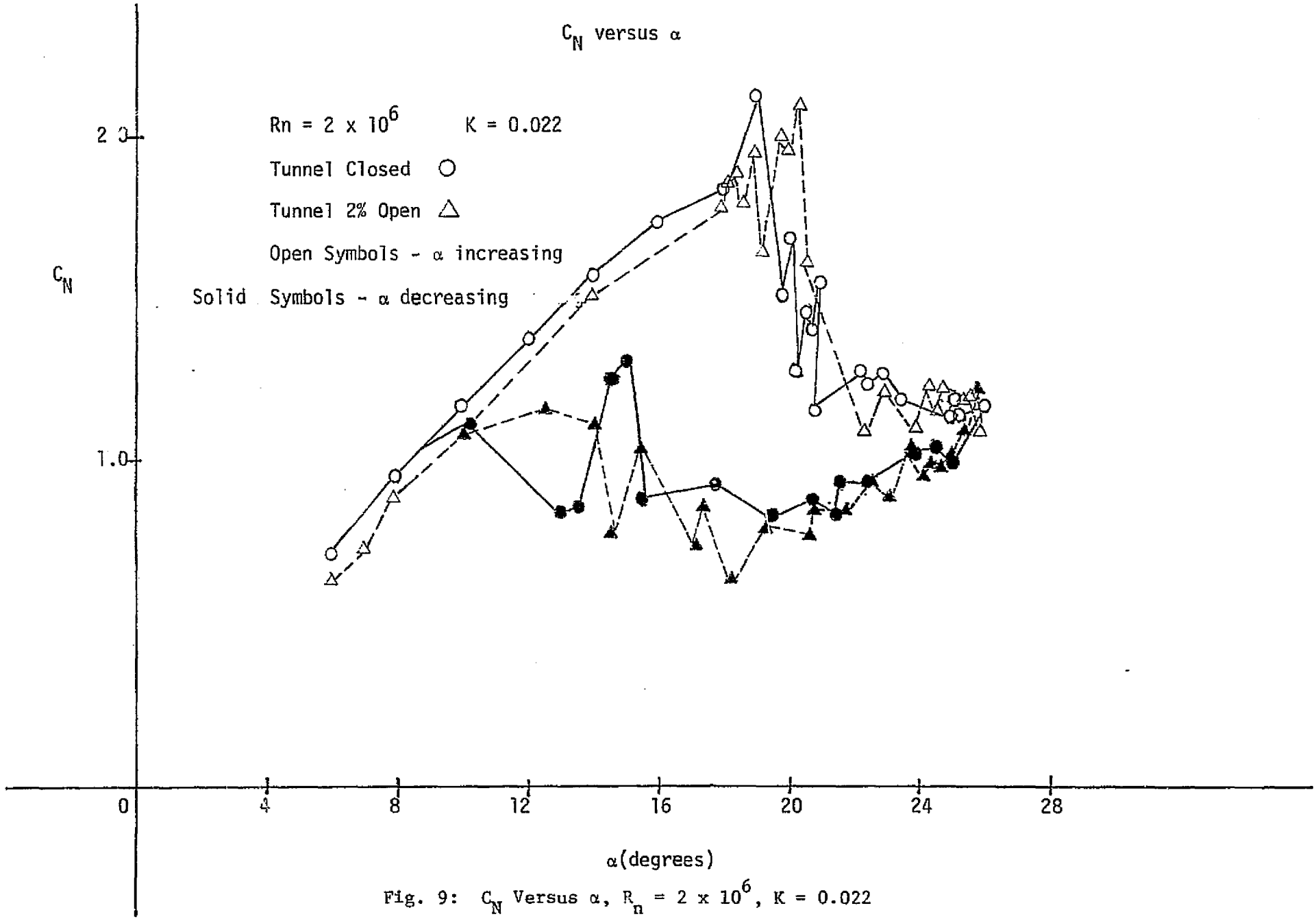

Fig. 9: C_N Versus α, R_n = 2 x 10^6, K = 0.022

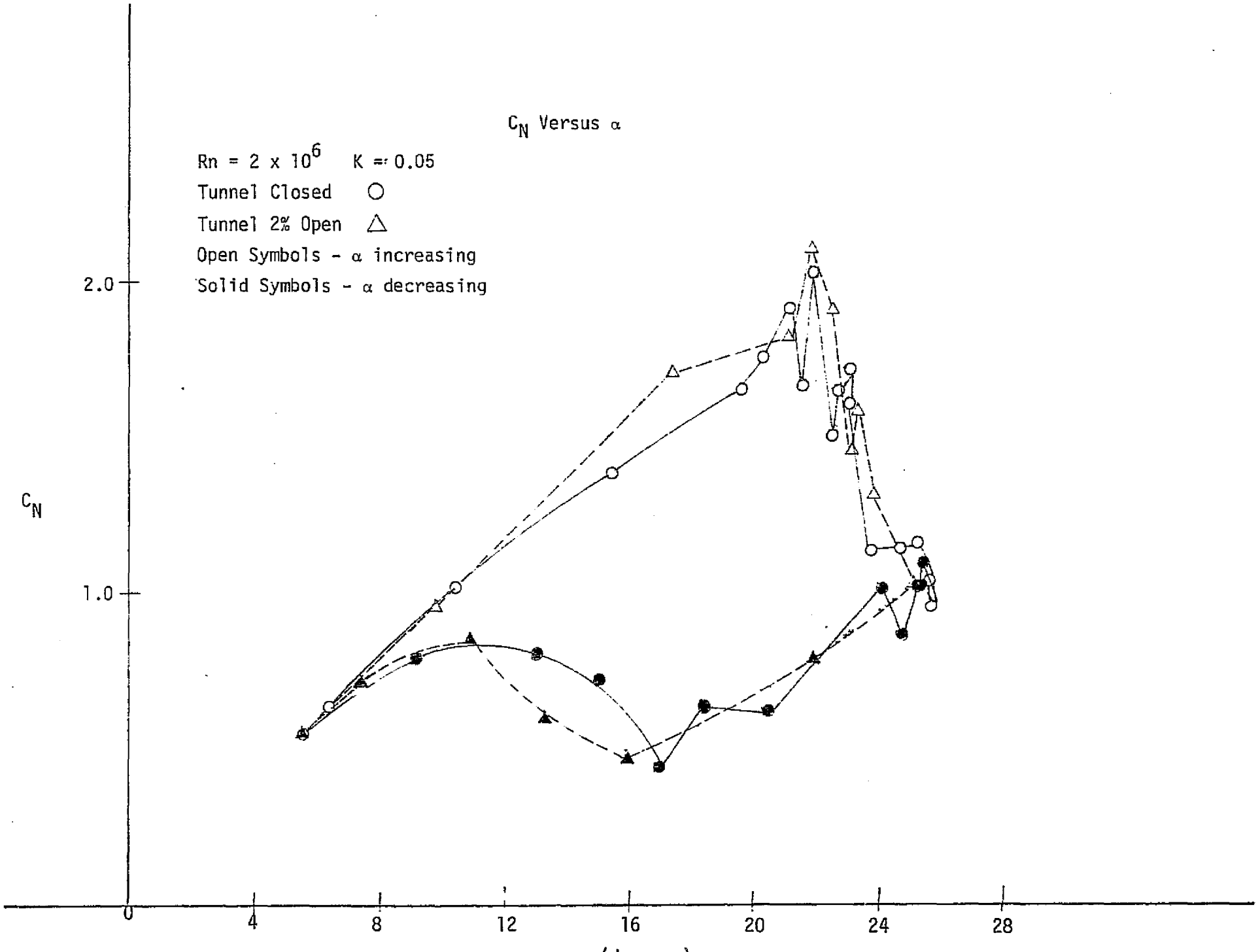

Fig. 10: C_N Versus α, R_n = 2 x 10^6, K = 0.05

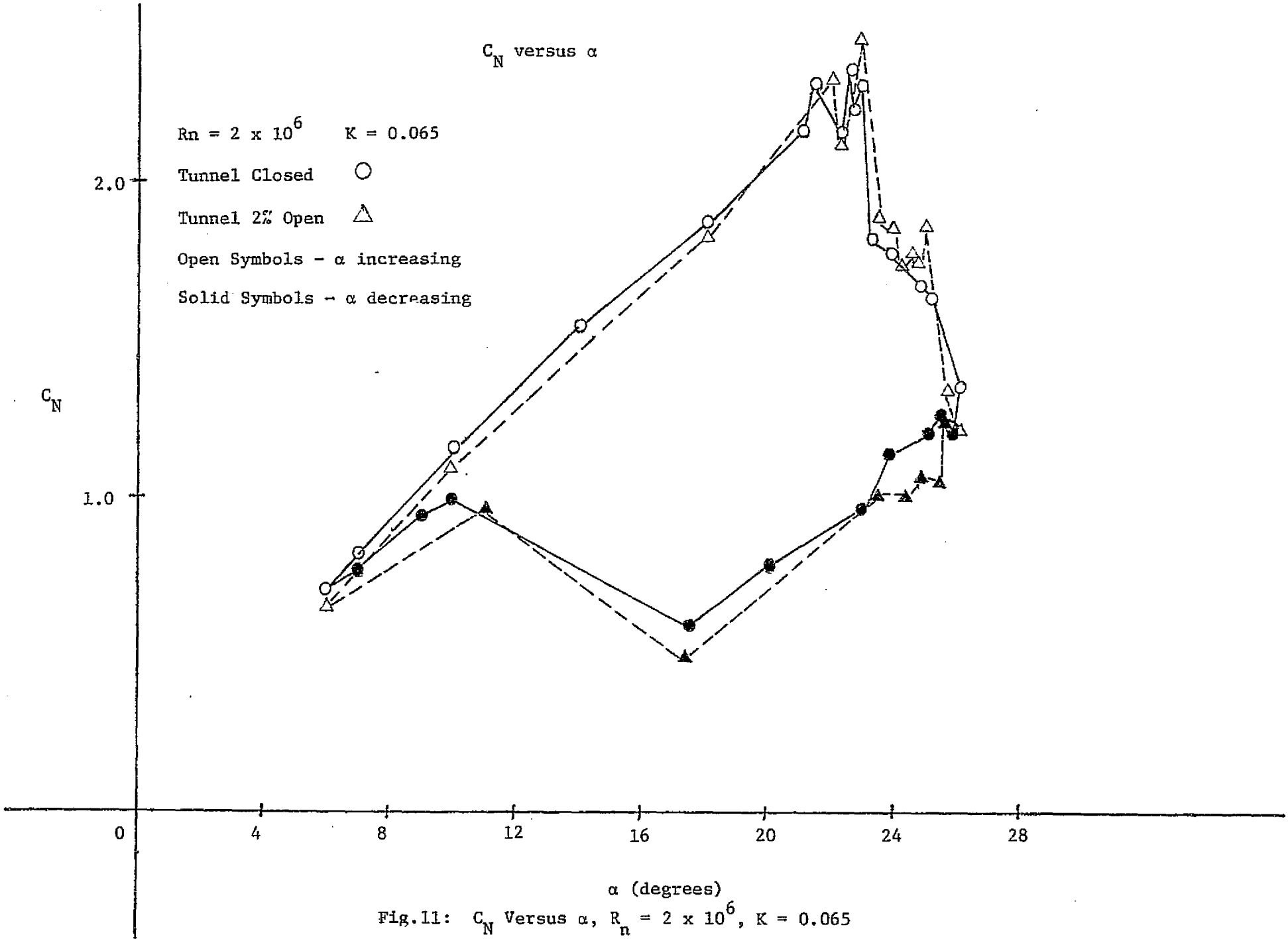

Fig.11: C_N Versus α, R_n = 2 x 10^6, K = 0.065

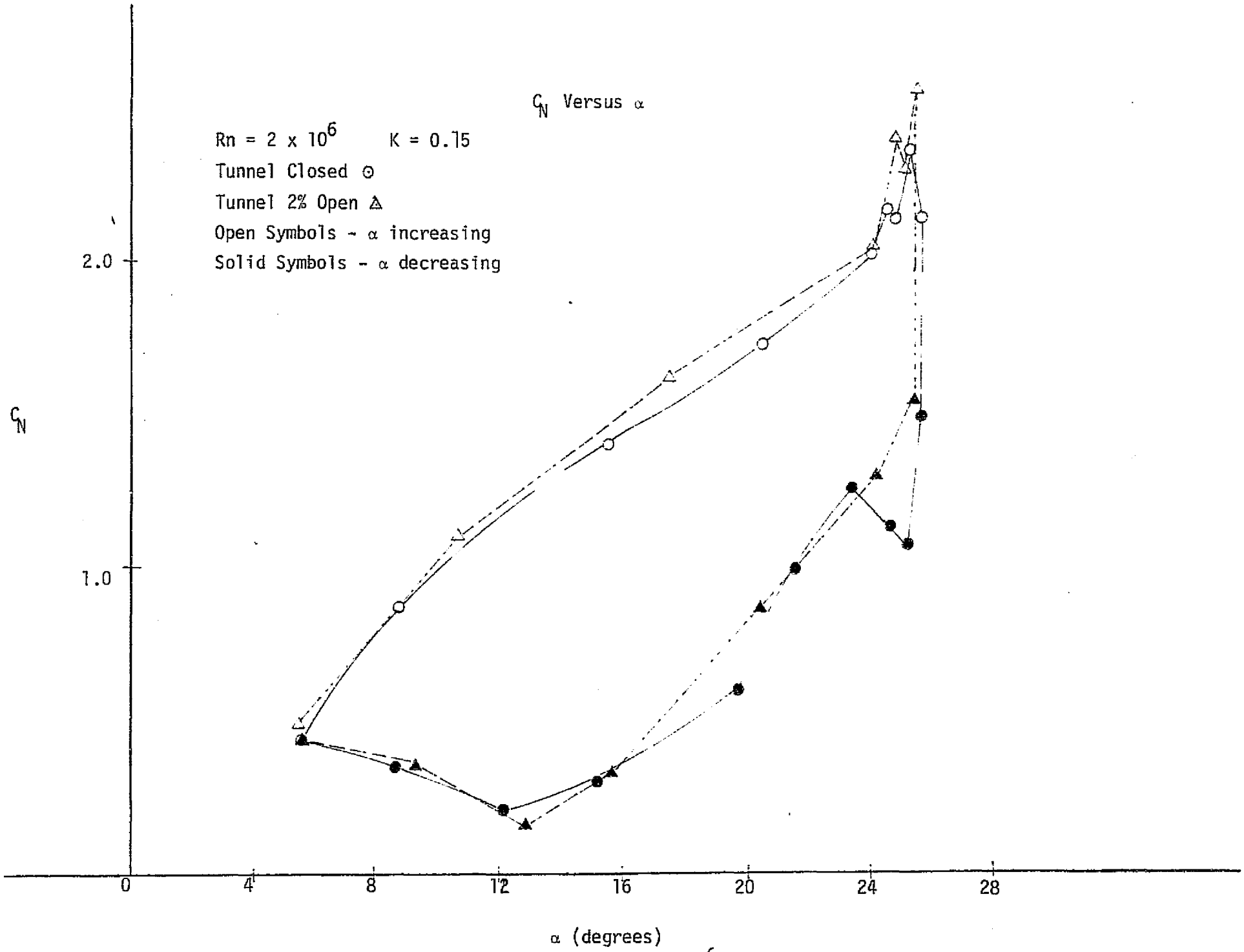

Fig. 12: C_N Versus α, R_n = 2 x 10^6, K = 0.15

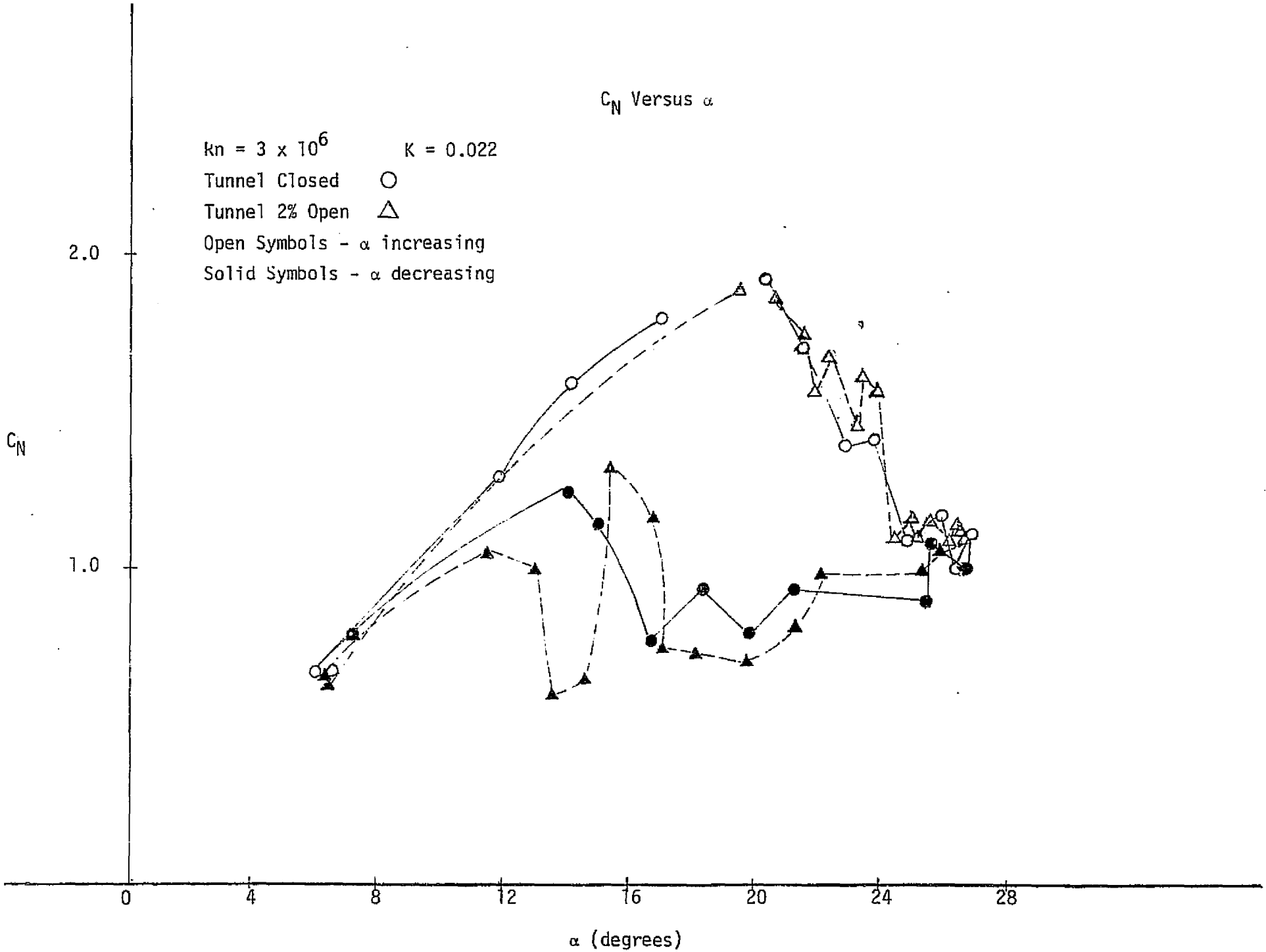

Fig. 13: C_N Versus α, R_n = 3 x 10^6, K = 0.022

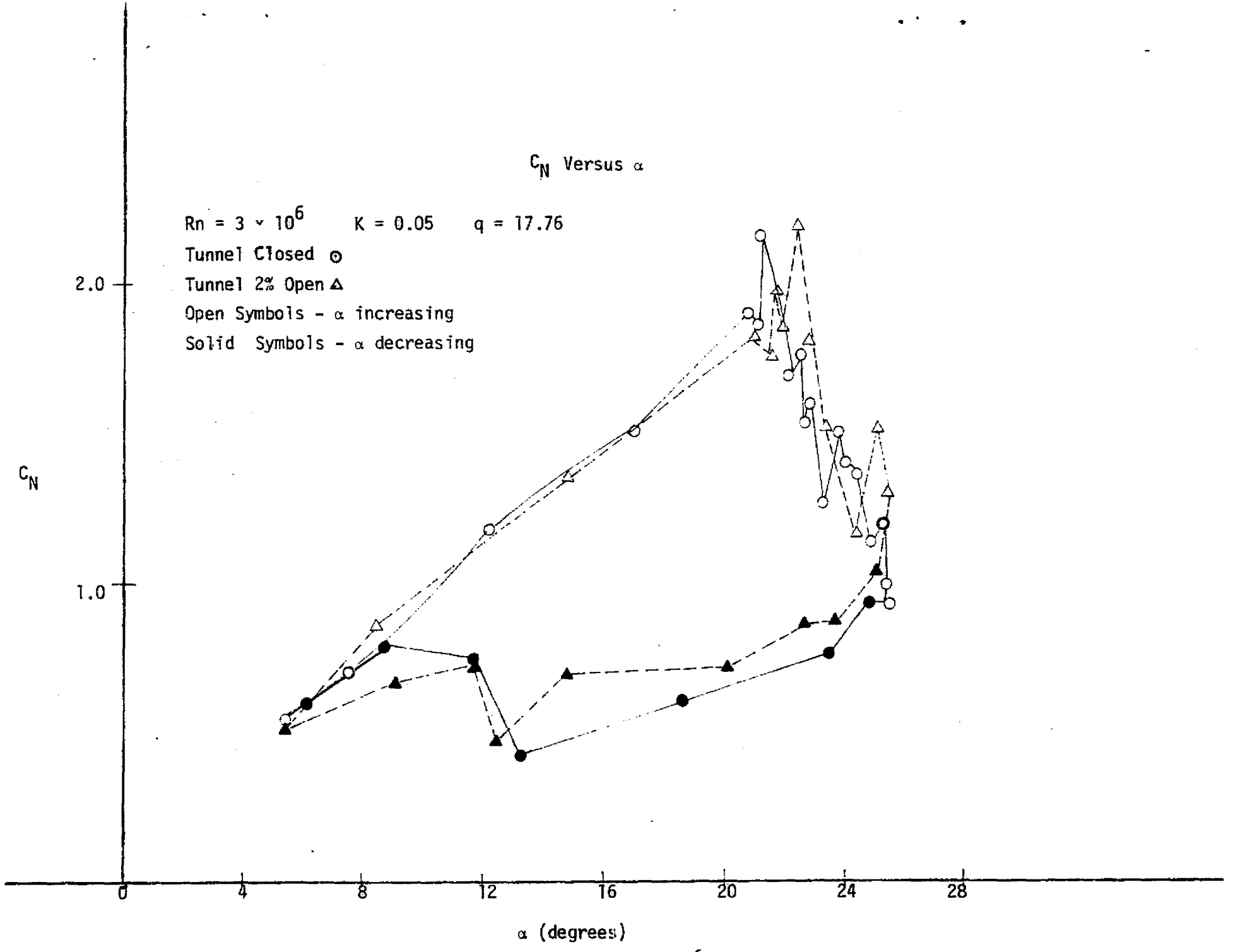

Fig. 14: C_N Versus α, $R_n = 3 \times 10^6$, K = 0.05

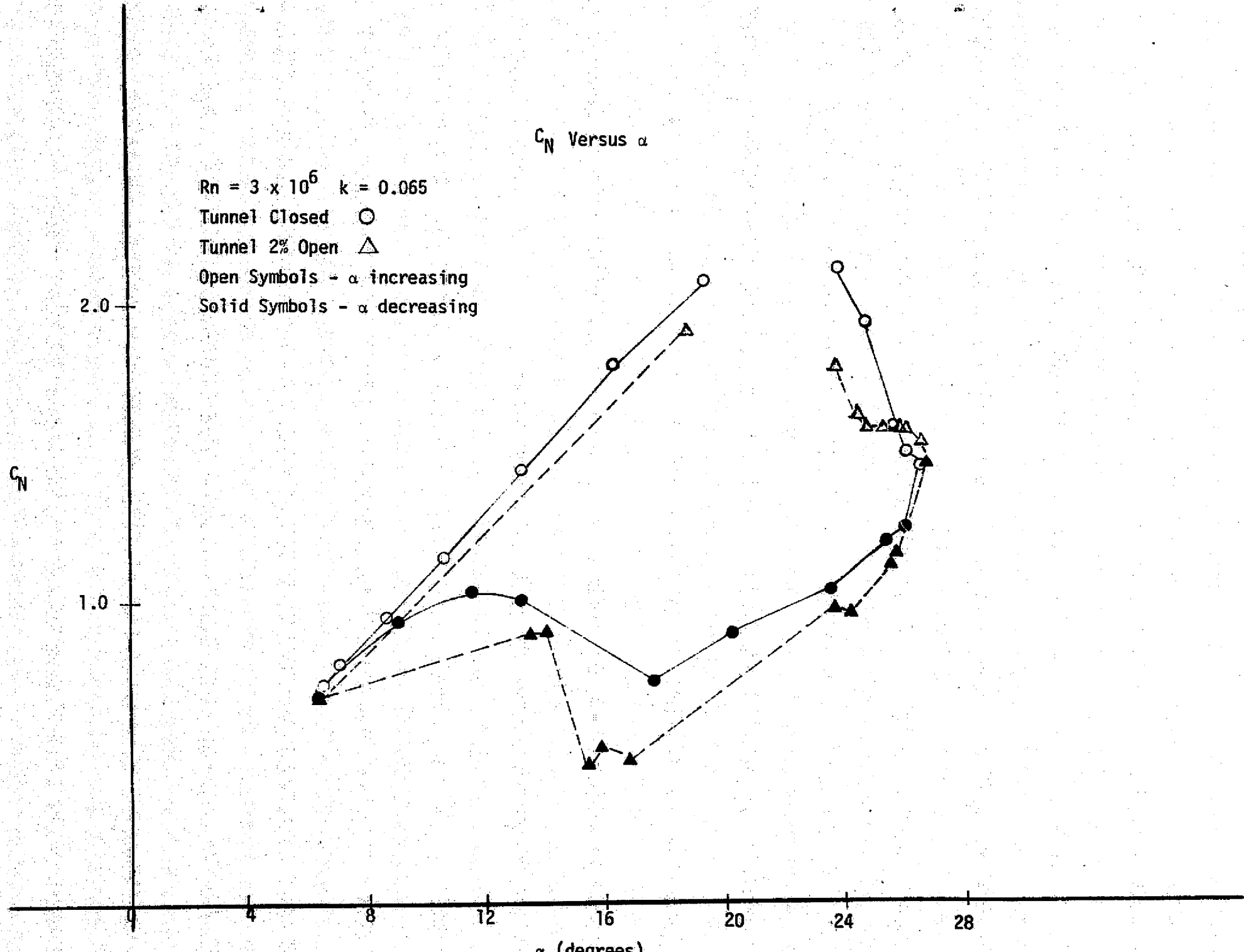

Fig. 15: C_N Versus α, R_n = 3 x 10^6, K = 0.065

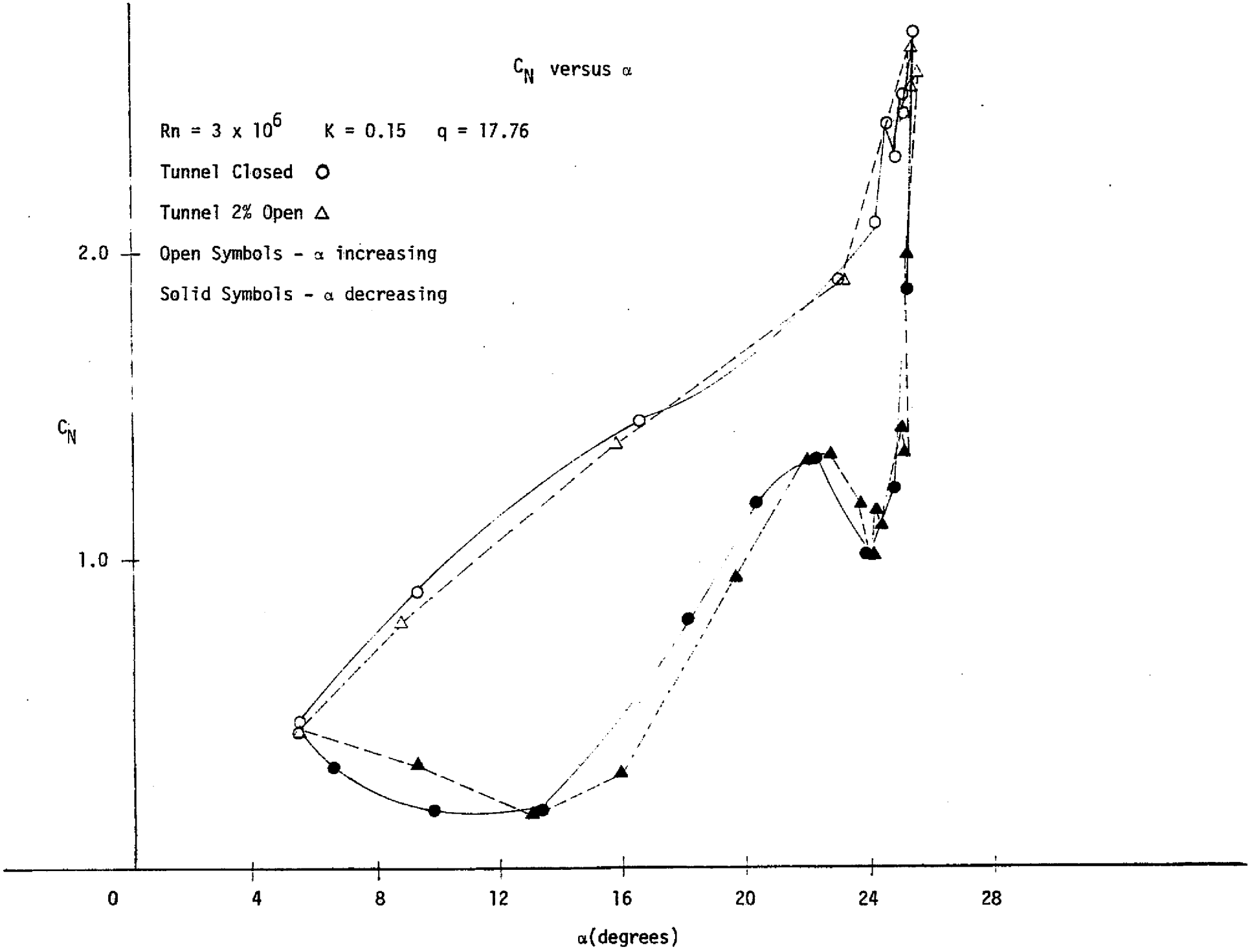
C_N versus α
Rn = 3 x 10^6 K = 0.15 q = 17.76
Tunnel Closed O
Tunnel 2% Open △
Open Symbols - α increasing
Solid Symbols - α decreasing
C_N
2.0
1.0
0
4
8
12
16
20
24
28
α(degrees)

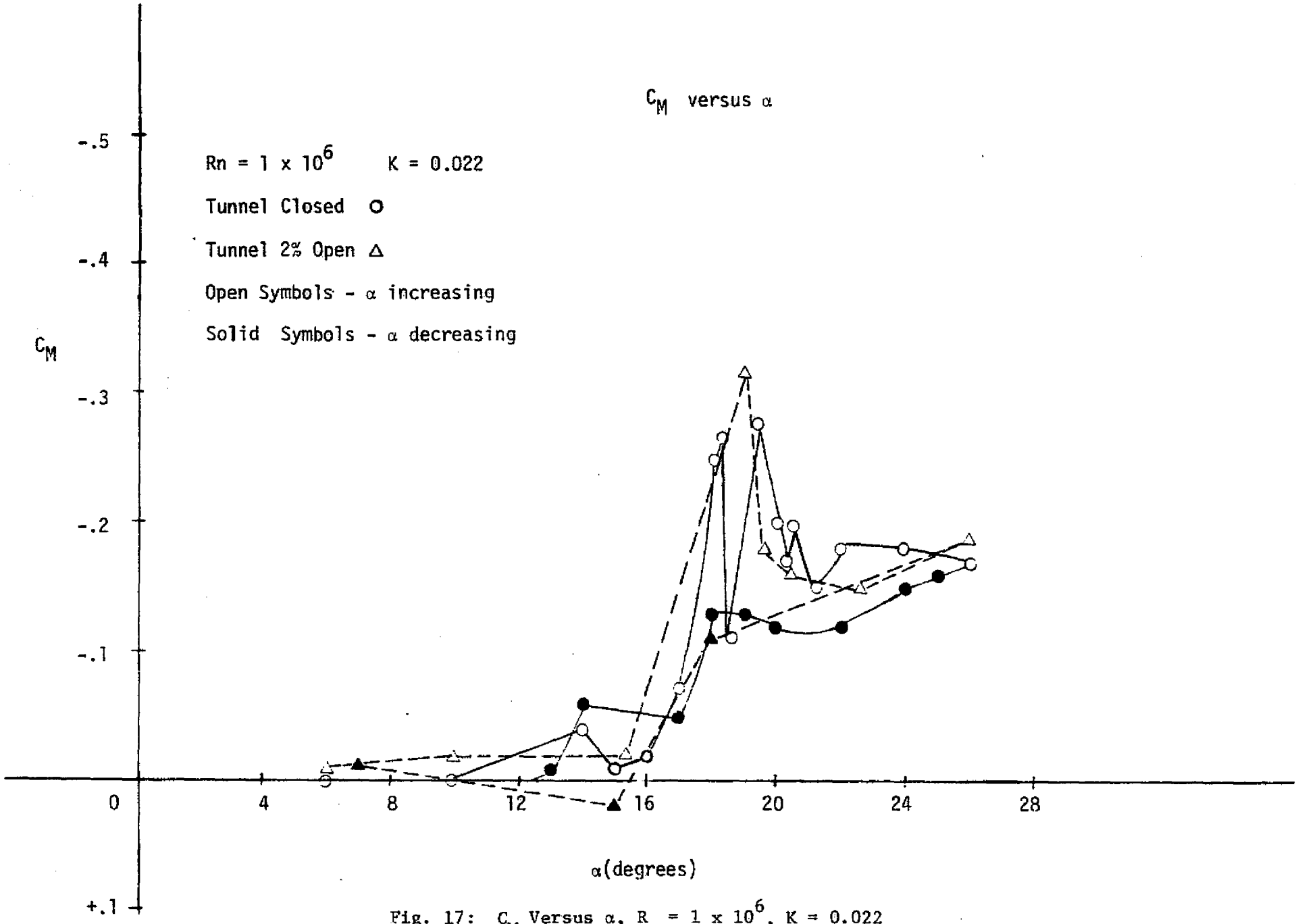

Fig. 17: C_M Versus α, $R_n = 1 \times 10^6$, K = 0.022

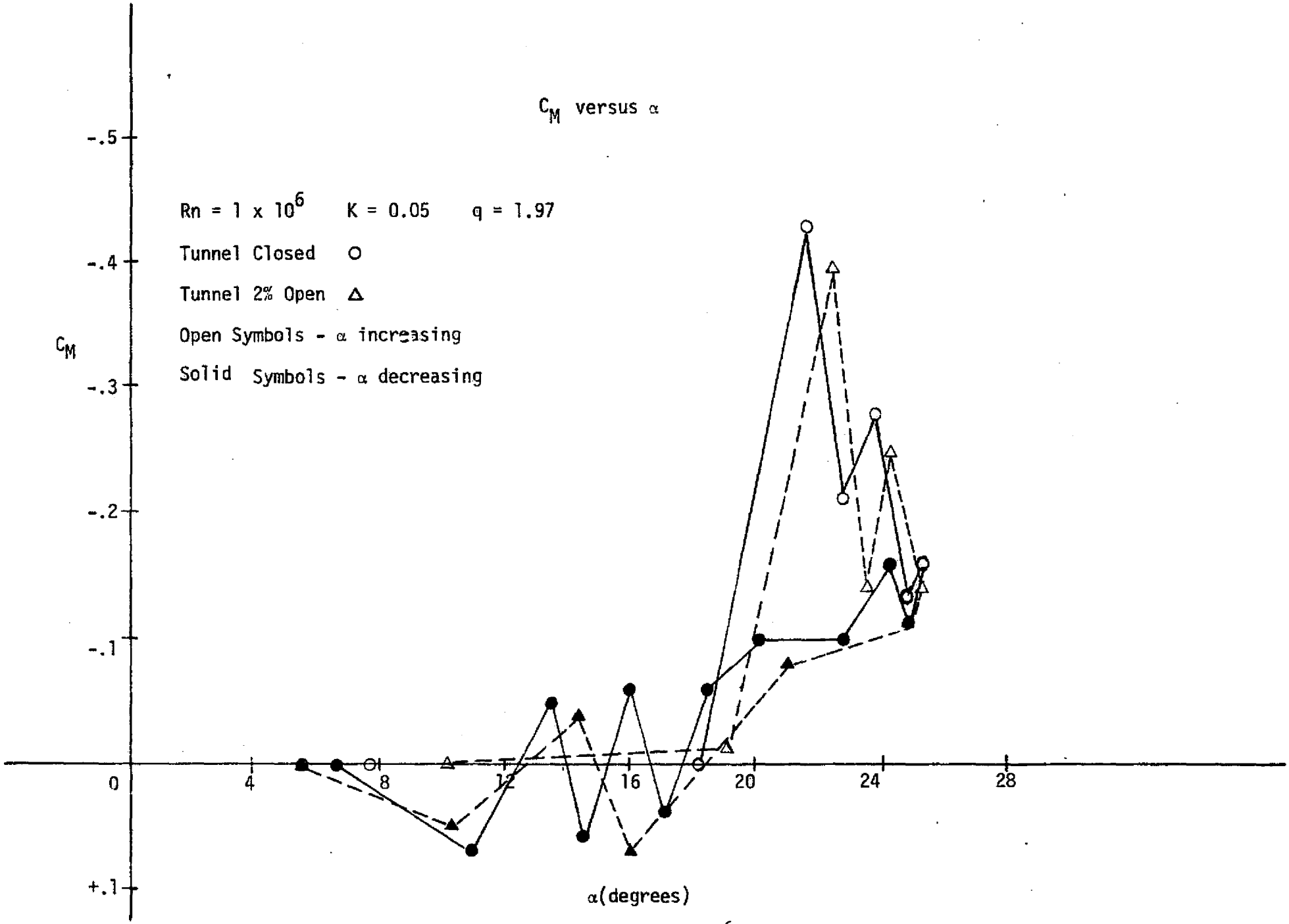

Fig. 18: C_M Versus α, R_n = 1 x 10^6, K = 0.05

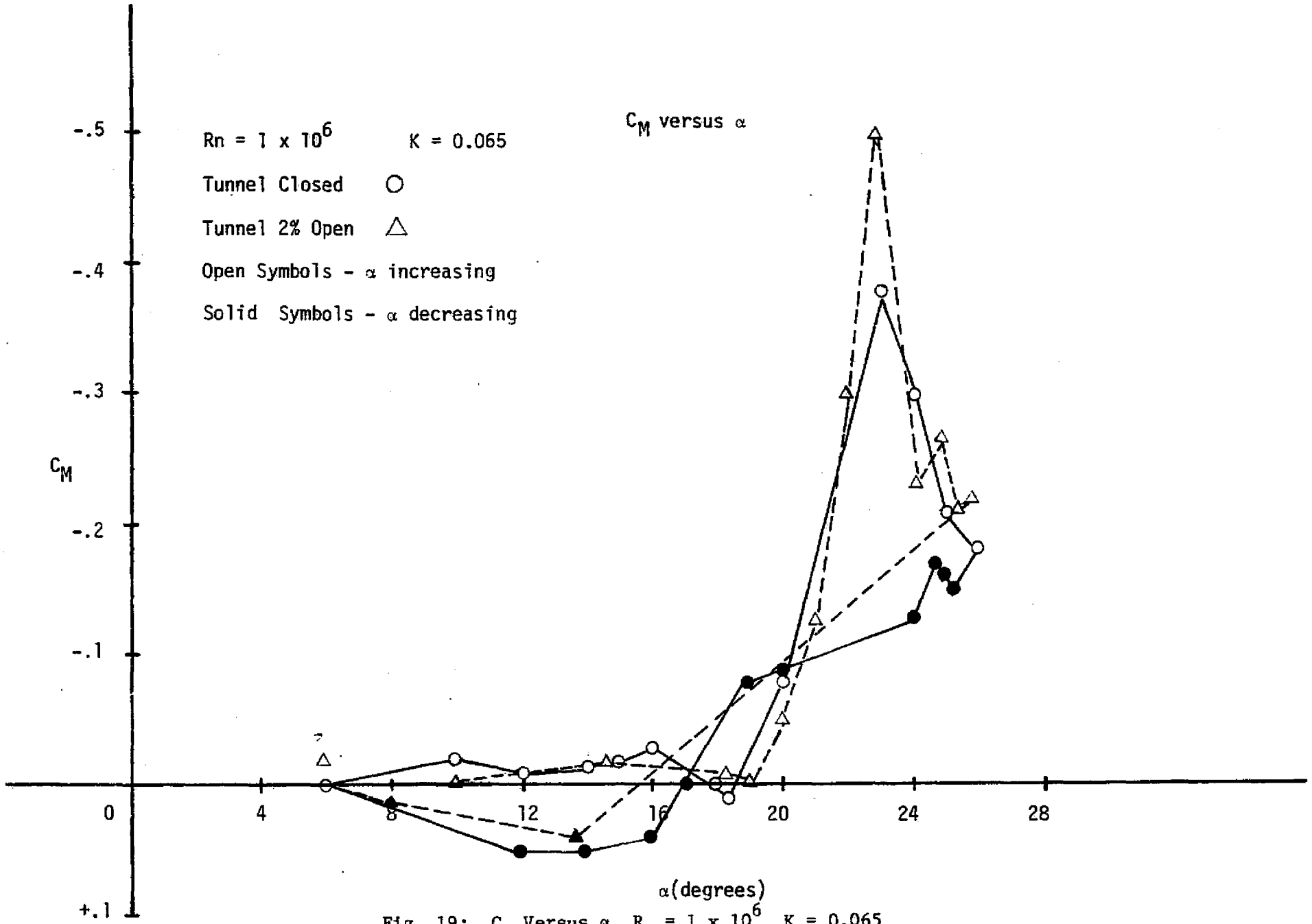

Fig. 19: C_M Versus α, R_n = 1 x 10^6, K = 0.065

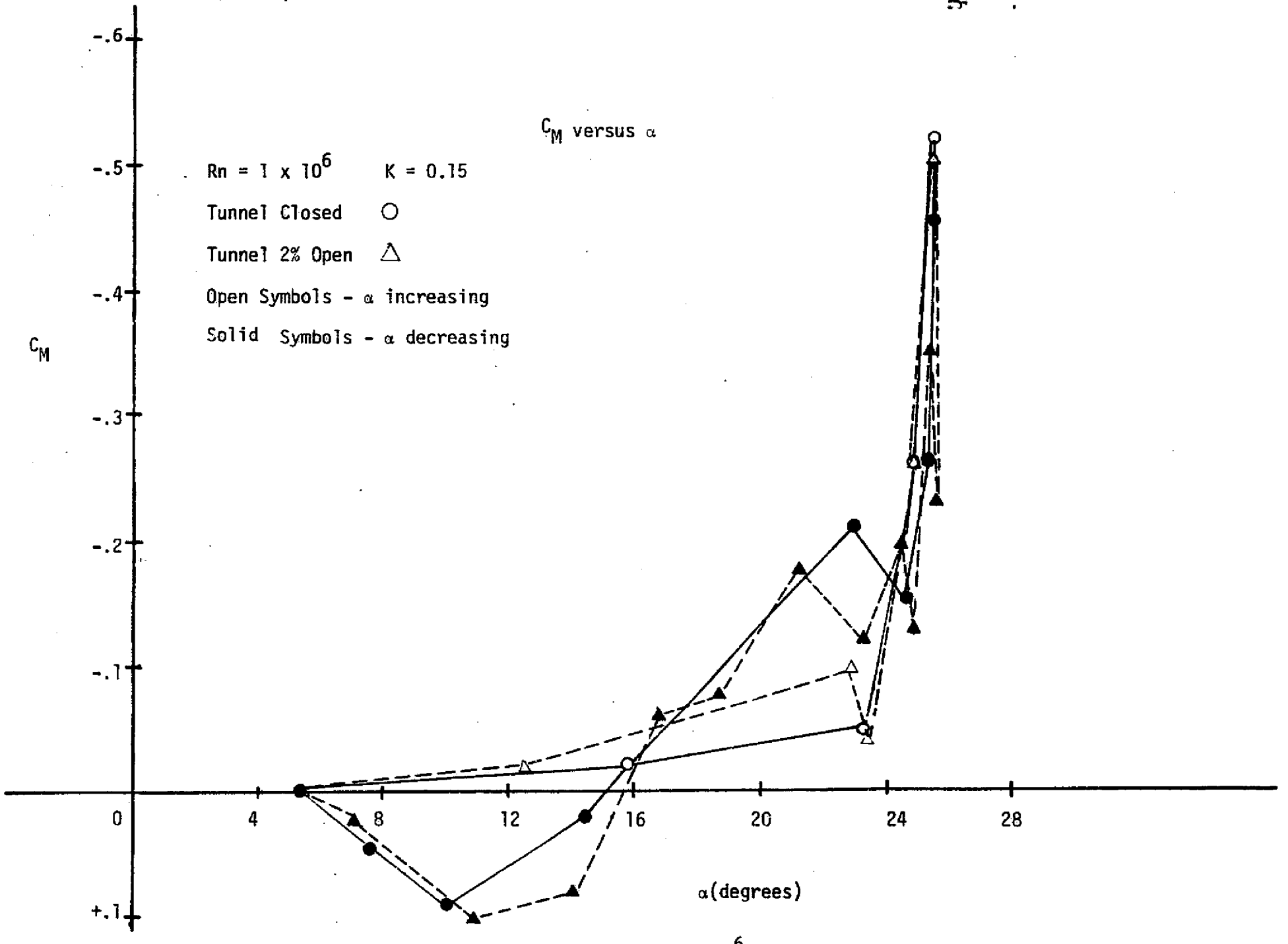

Fig. 20: C_M Versus α, R_n = 1 x 10^6, K = 0.15

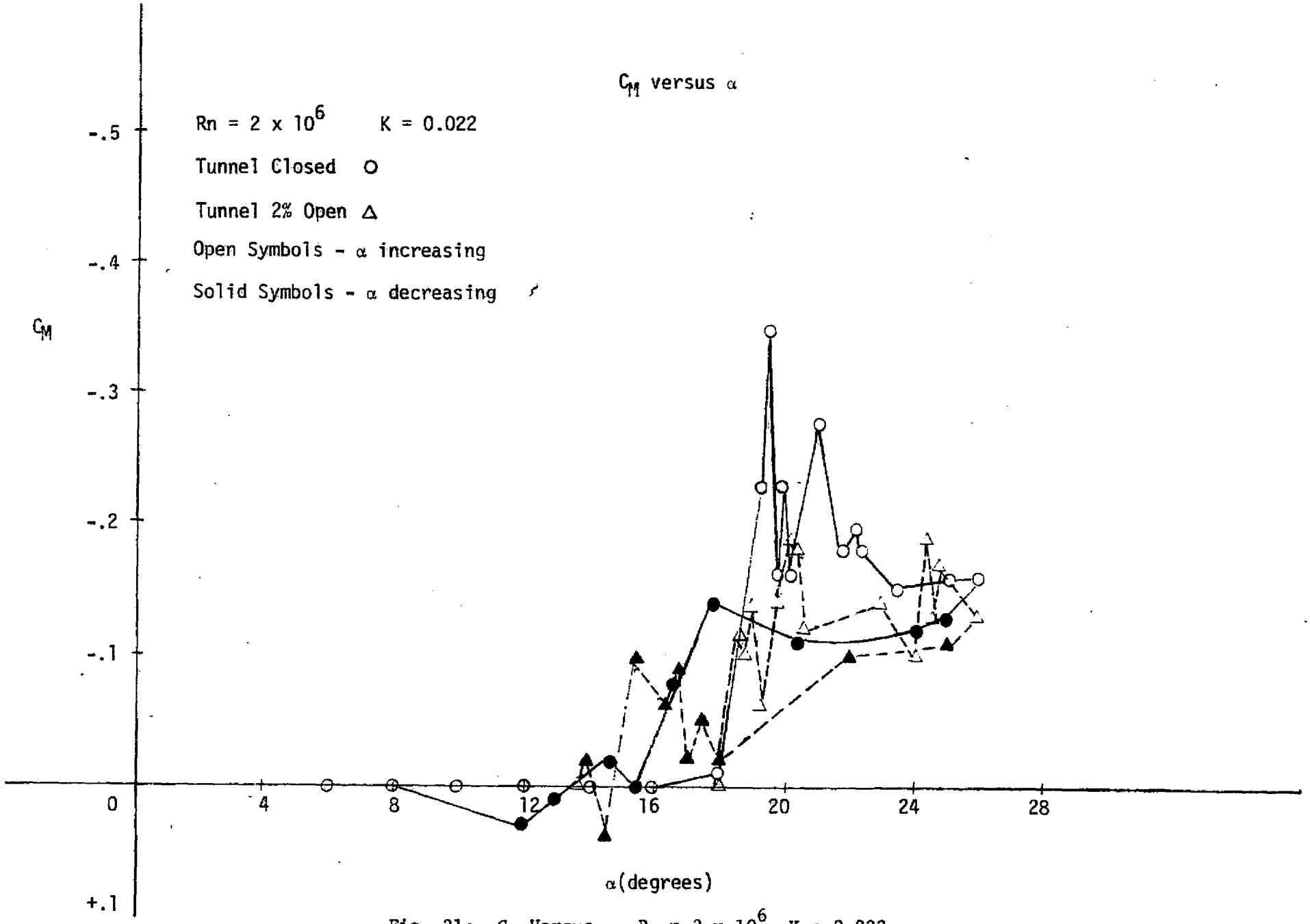

Fig. 21: C_M Versus α, $R_n = 2 \times 10^6$, K = 0.022

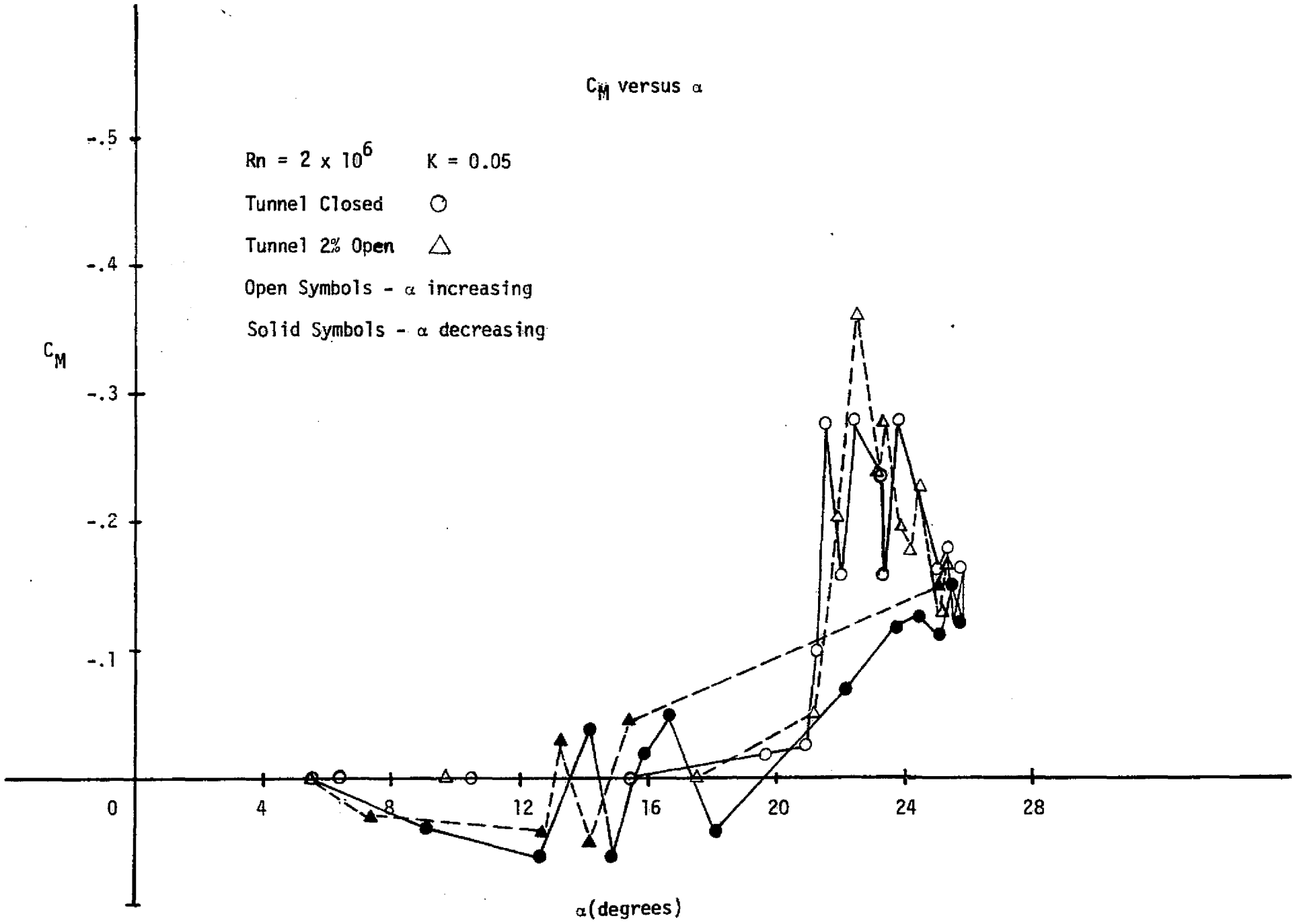

Fig. 22: C_M Versus α, $R_n = 2 \times 10^6$, K = 0.05

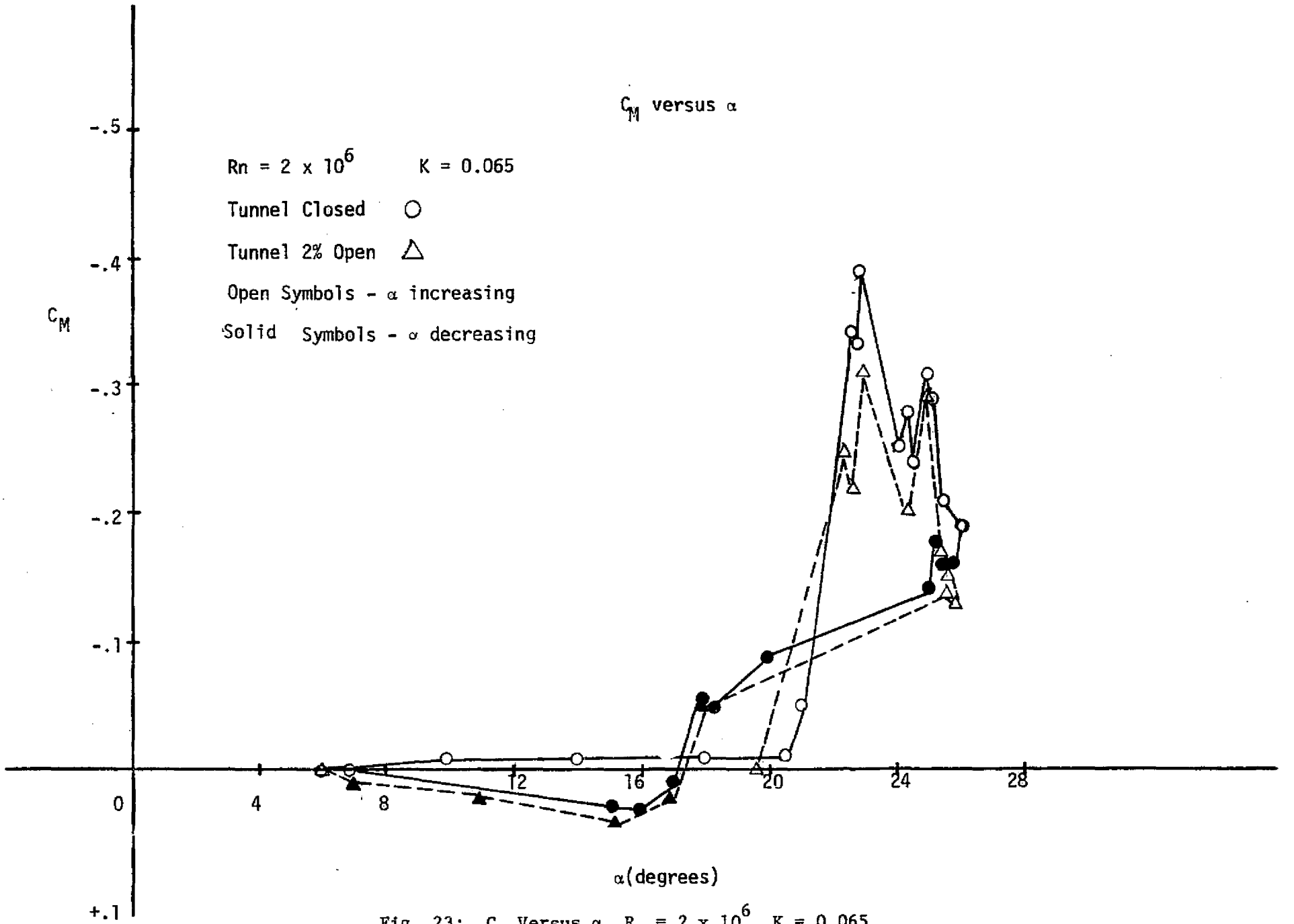

Fig. 23: C_M Versus α, $R_n = 2 \times 10^6$, K = 0.065

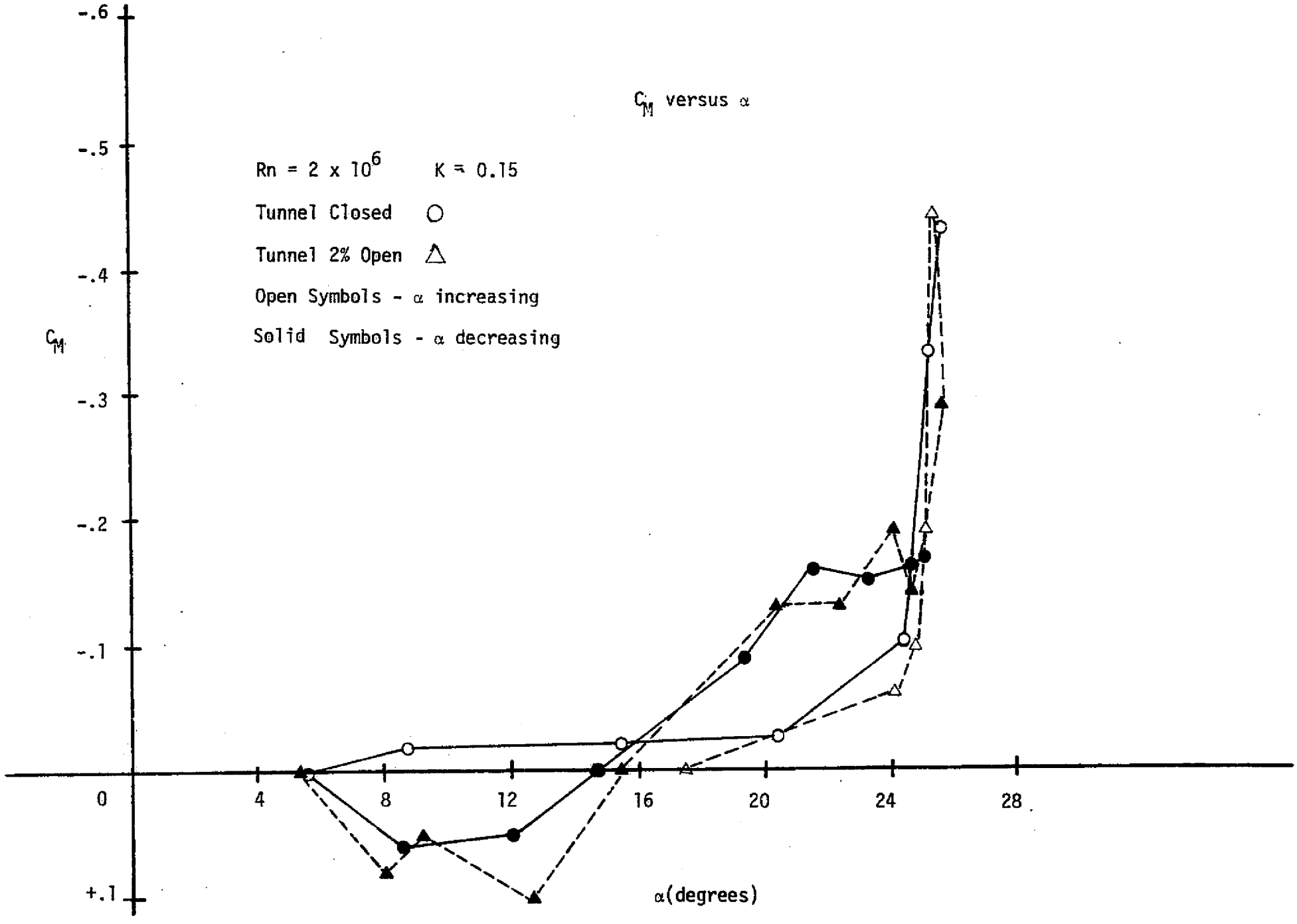

Fig. 24: C_M Versus α, R_n = 2 x 10^6, K = 0.15

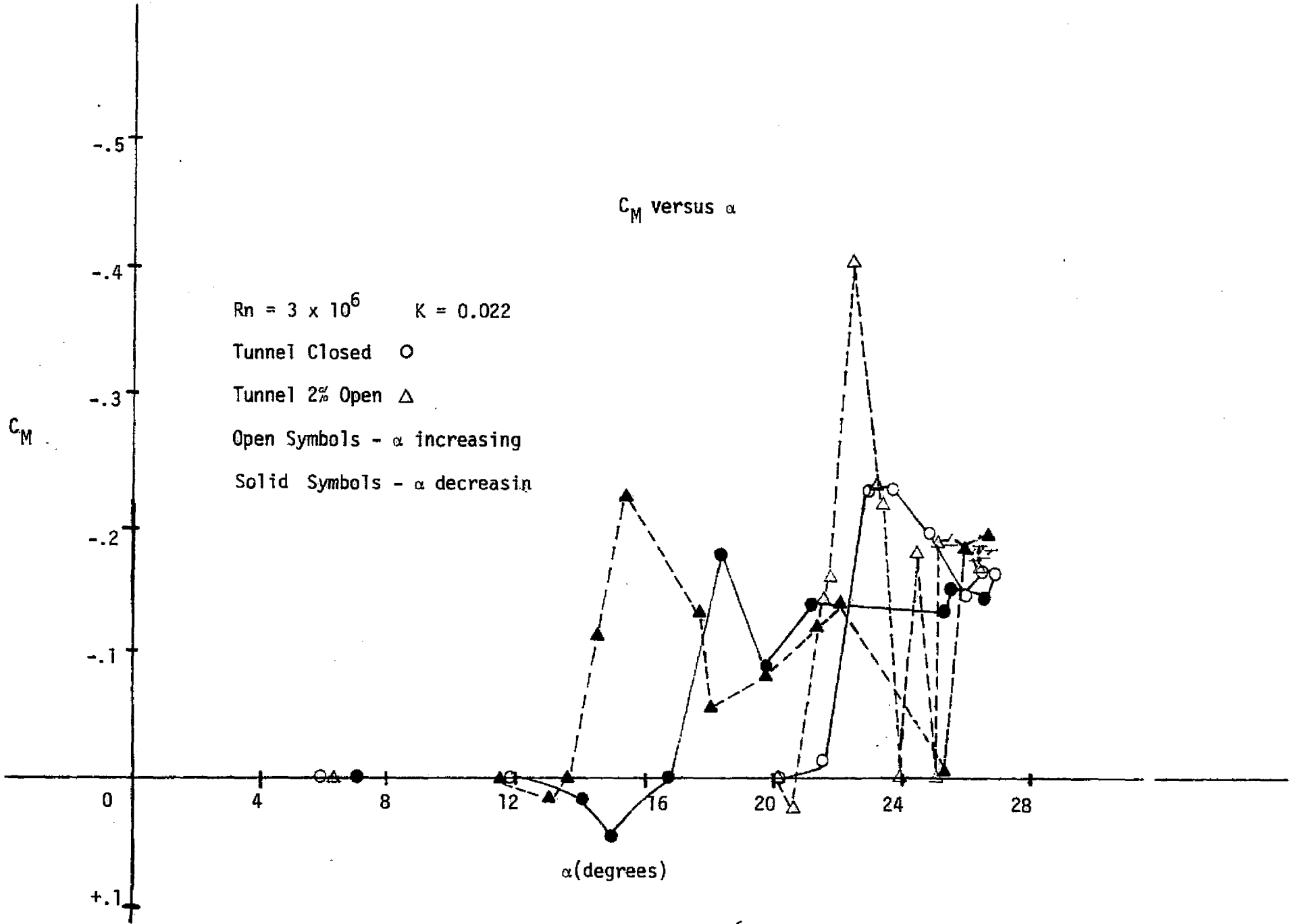

Fig. 25: C_M Versus α, R_n = 3 x 10^6, K = 0.022

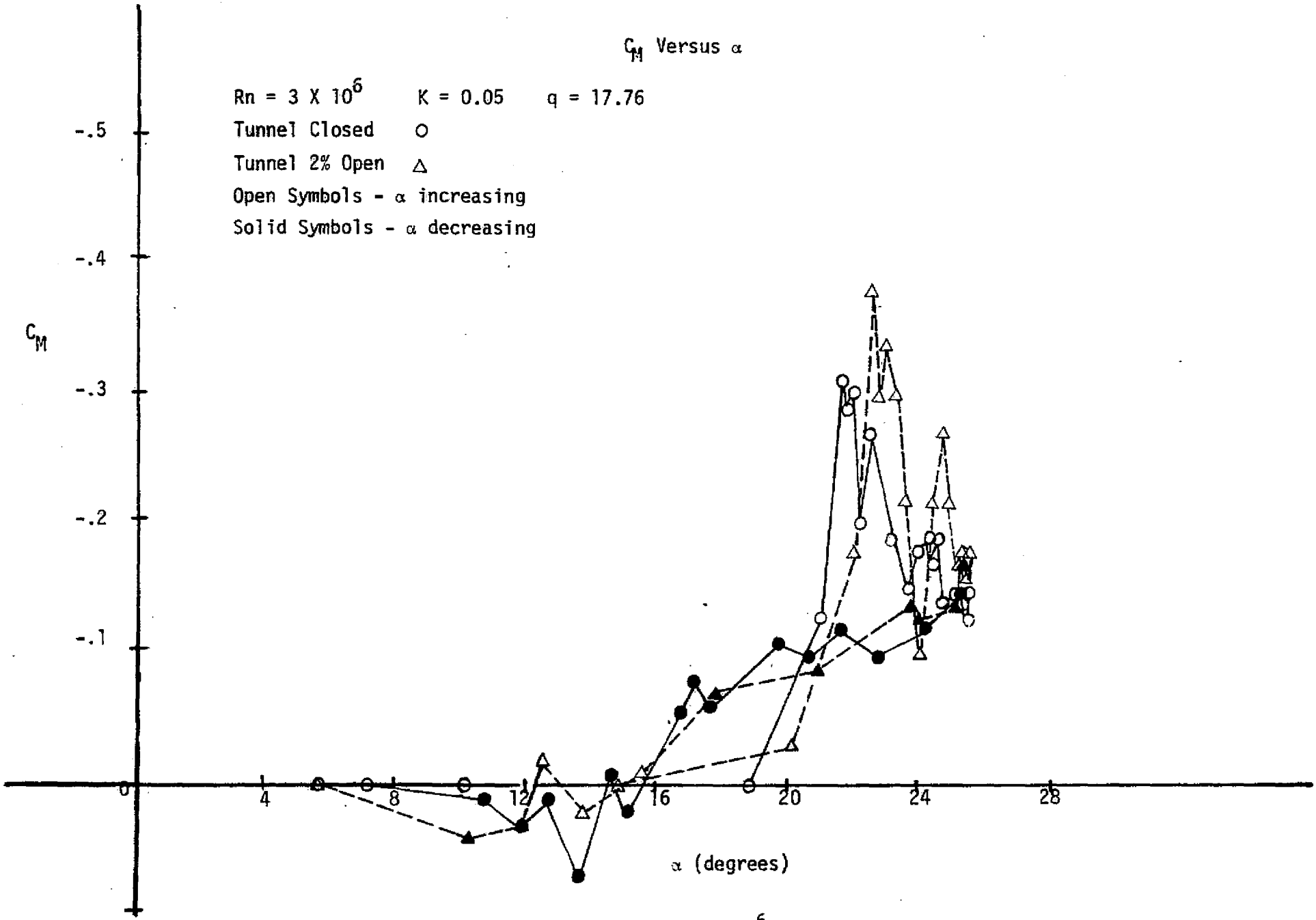

Fig. 26: C_M Versus α, R_n = 3 x 10^6, K = 0.05

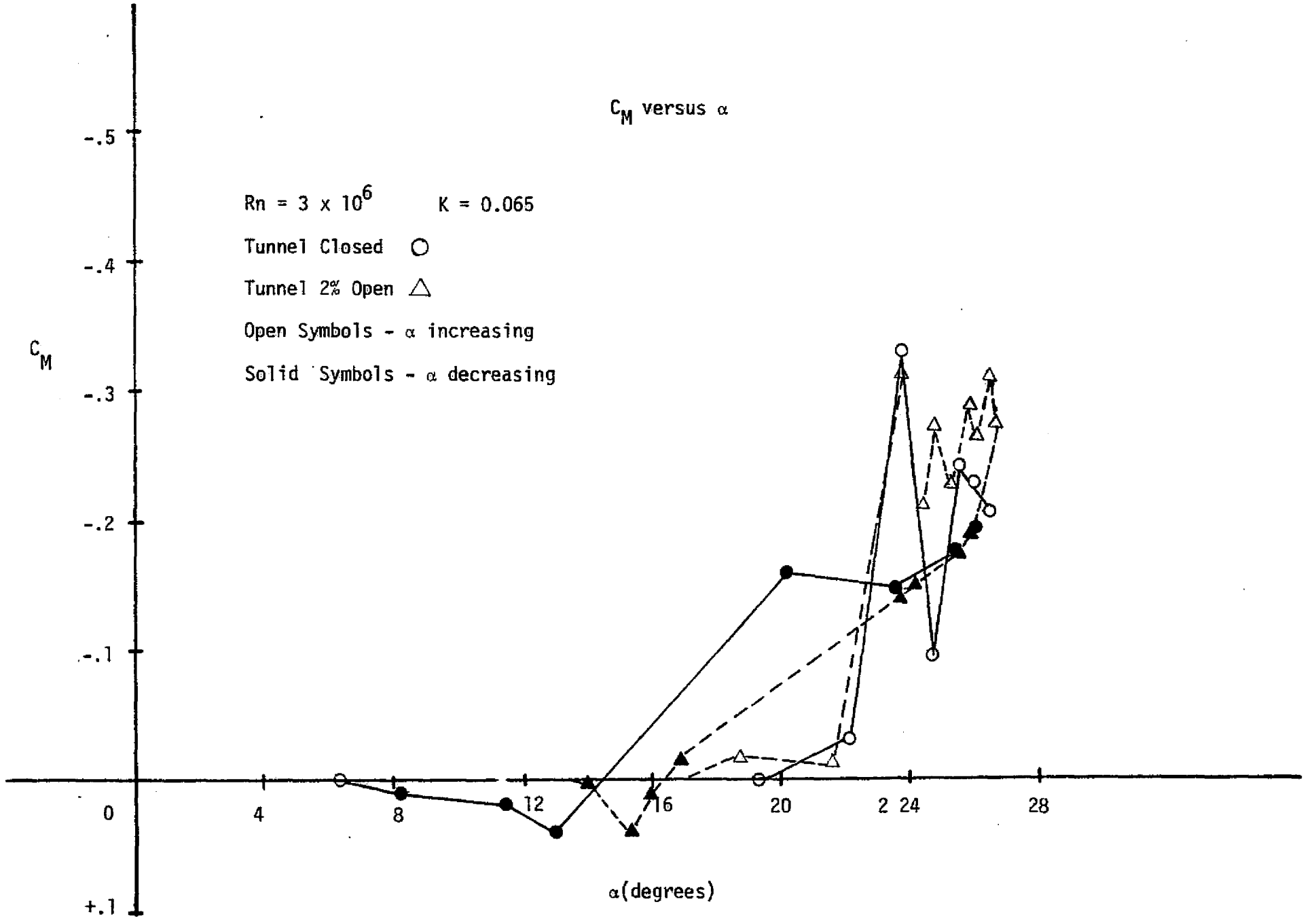

Fig. 27: C_M Versus α, R_n = 3 x 10^6, K = 0.065

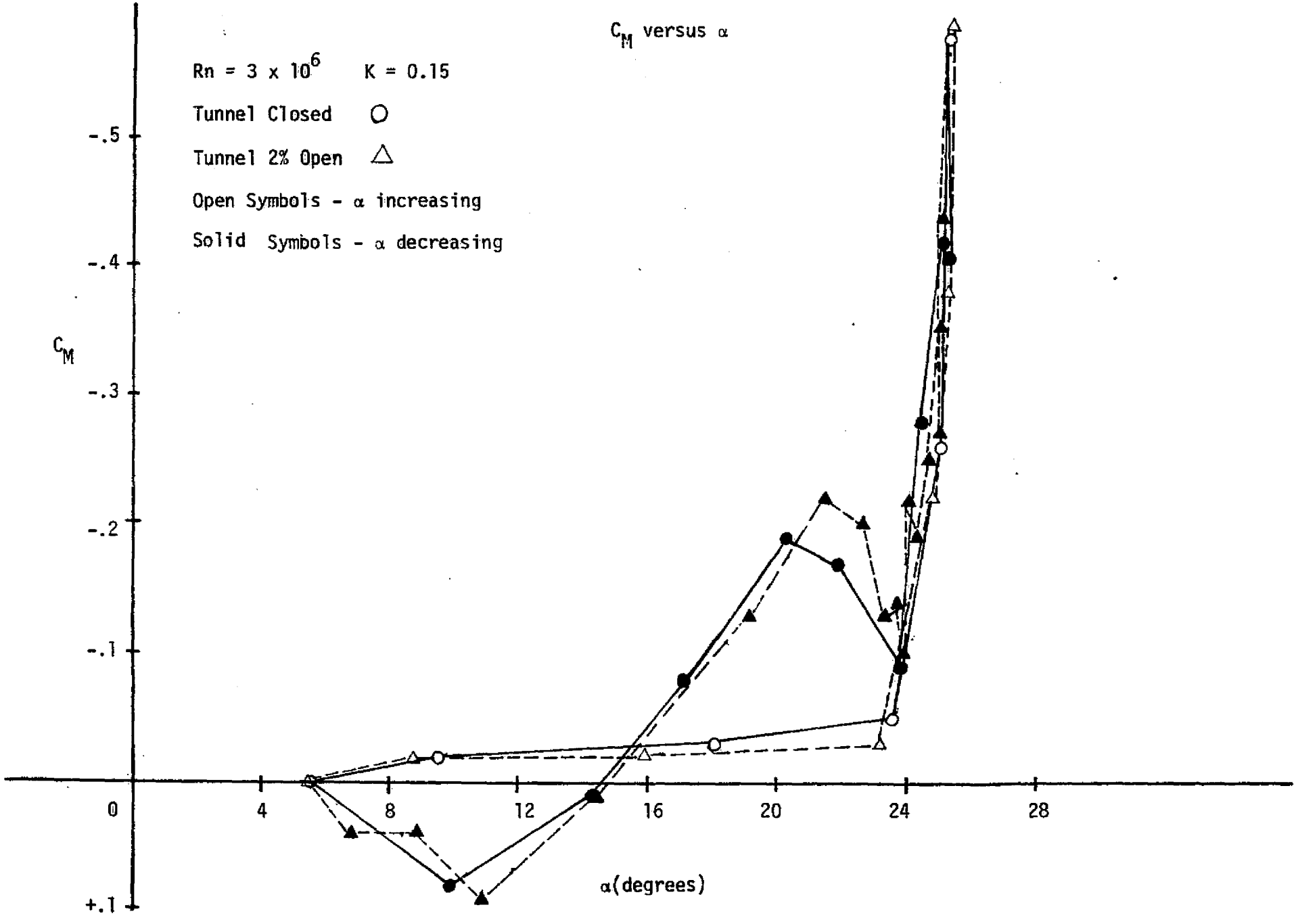

Fig. 28: C_M Versus α, R_n = 3 x 10^6, K = 0.15

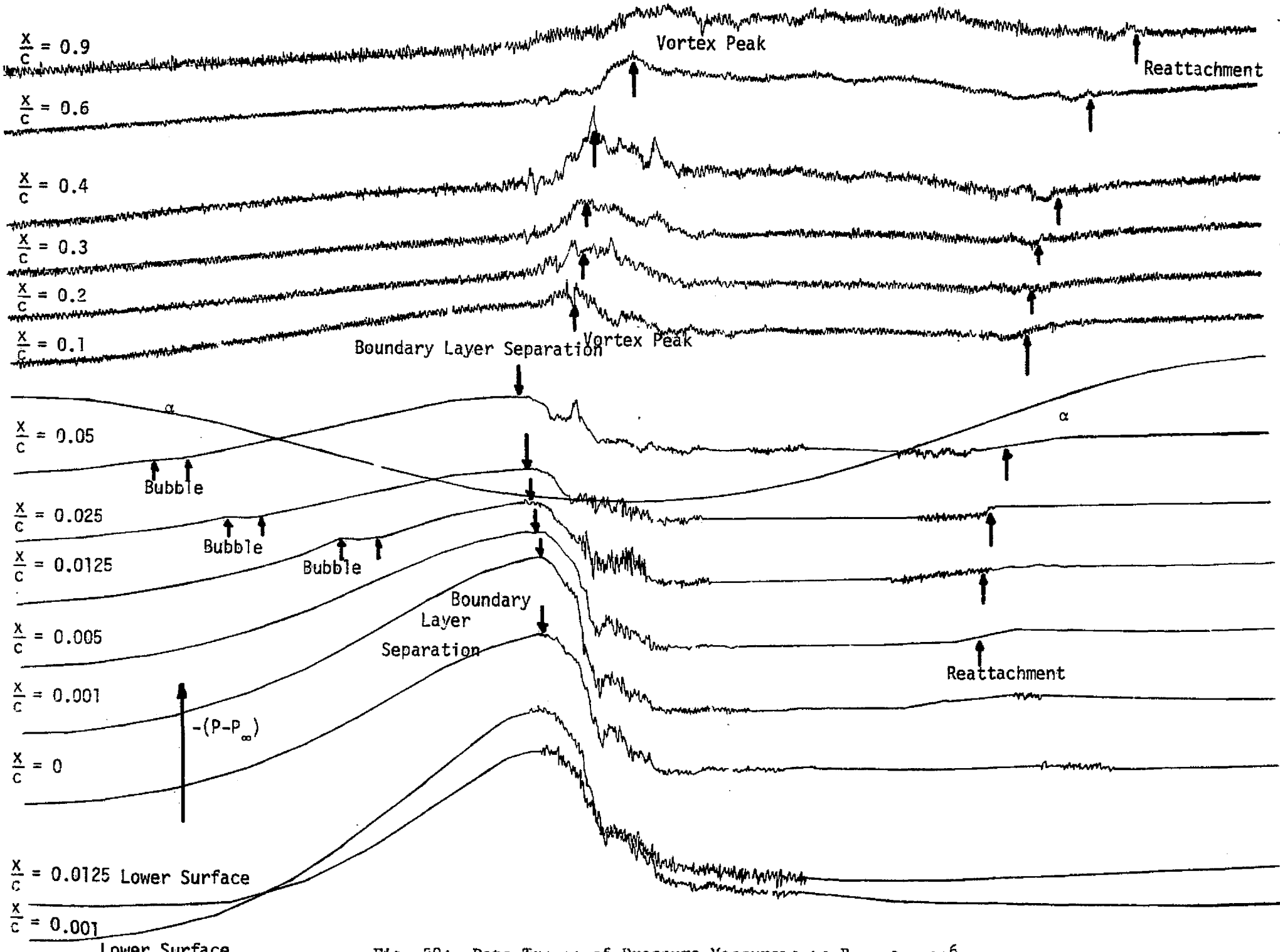

Fig. 29· Data Traces of Pressure Measurements $R_{\ell} = 2 \times 10^6$, $\alpha = 0.15$

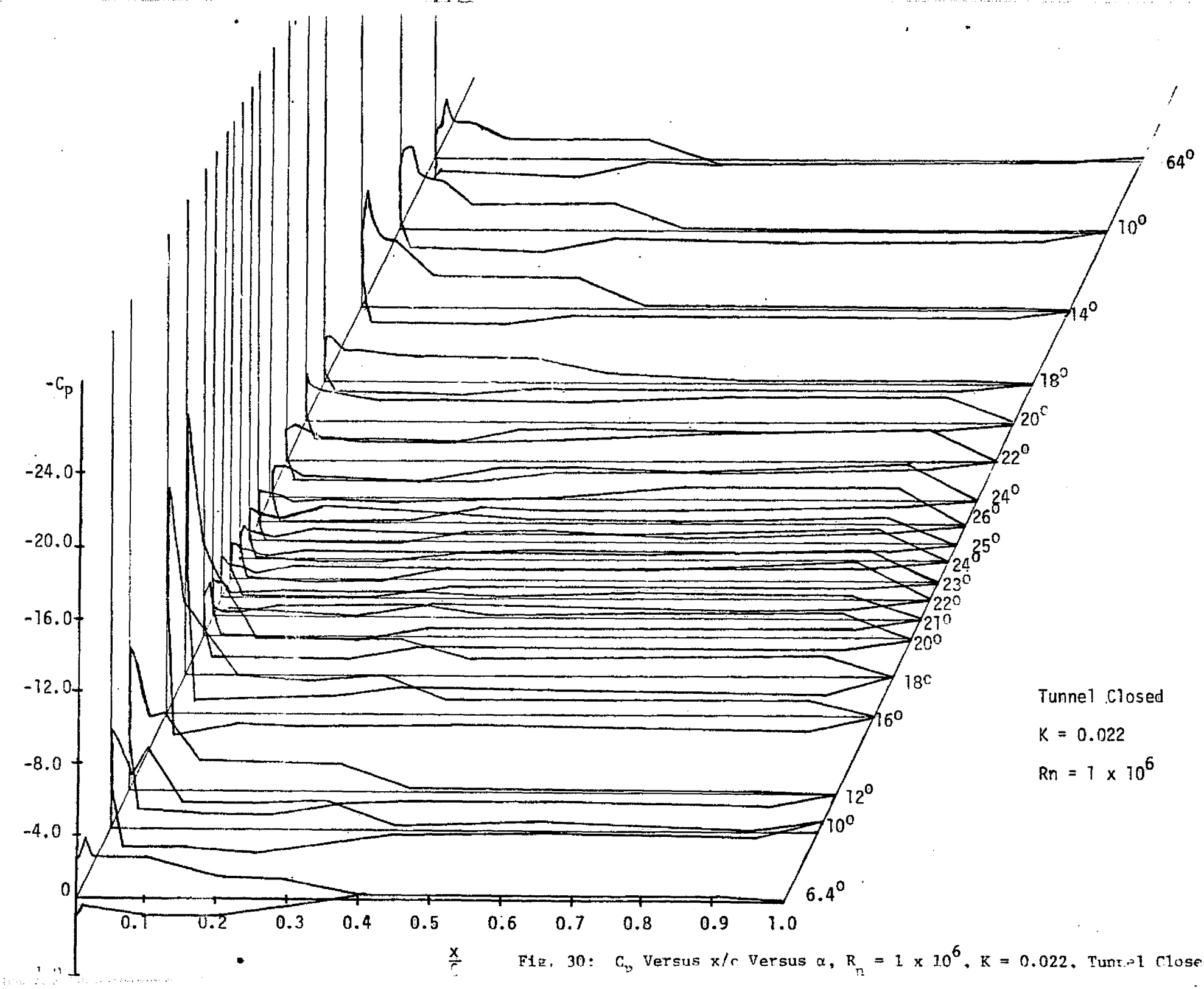

Fig. 30: C_p Versus x/c Versus α, $R_n = 1 \times 10^6$, K = 0.022, Tunnel Closed

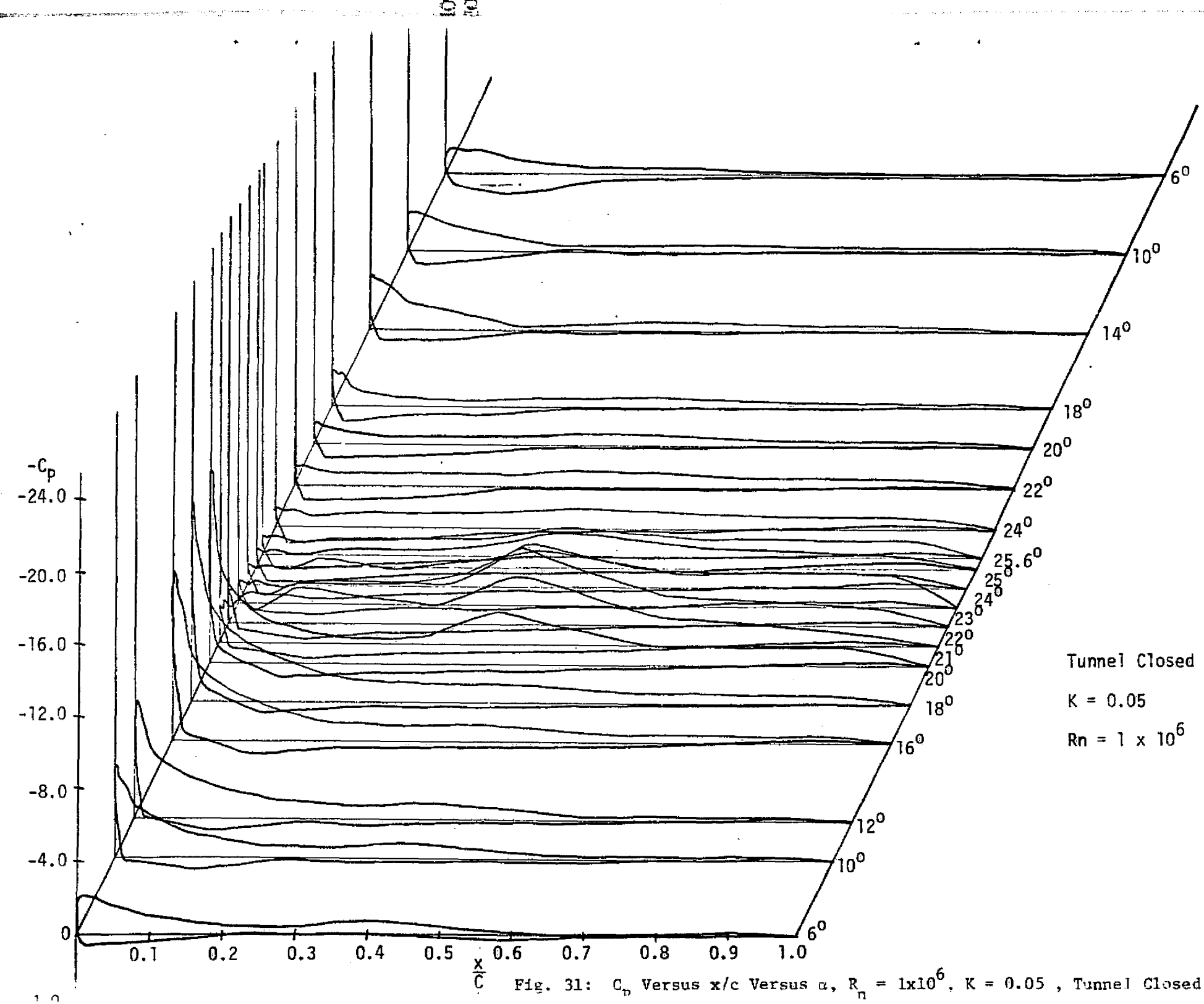

Fig. 31: C_p Versus x/c Versus α, $R_n = 1 \times 10^6$, K = 0.05 , Tunnel Closed

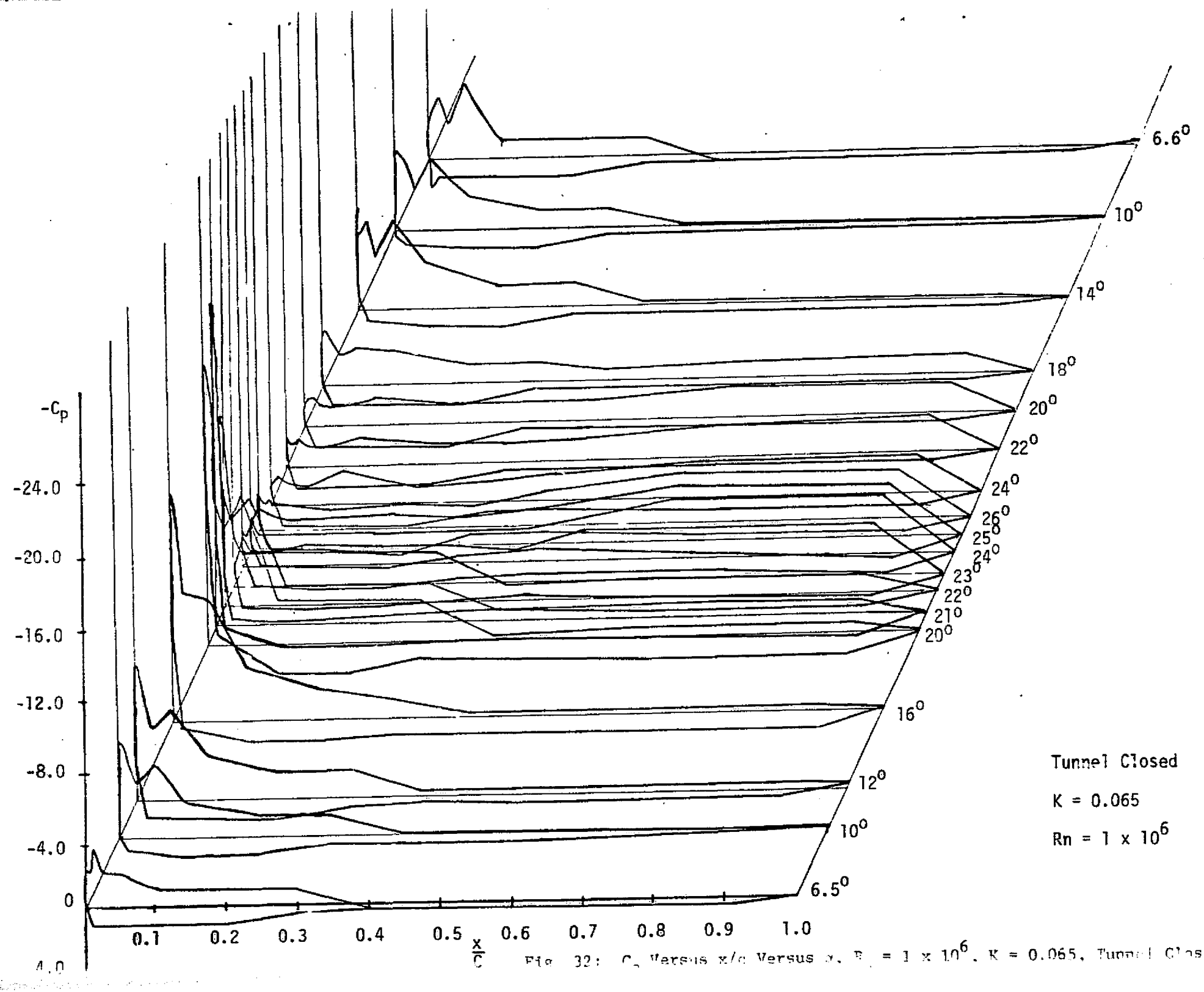

Fig. 32: C_p Versus x/c Versus α, R_n = 1 x 10^6, K = 0.065, Tunnel Closed

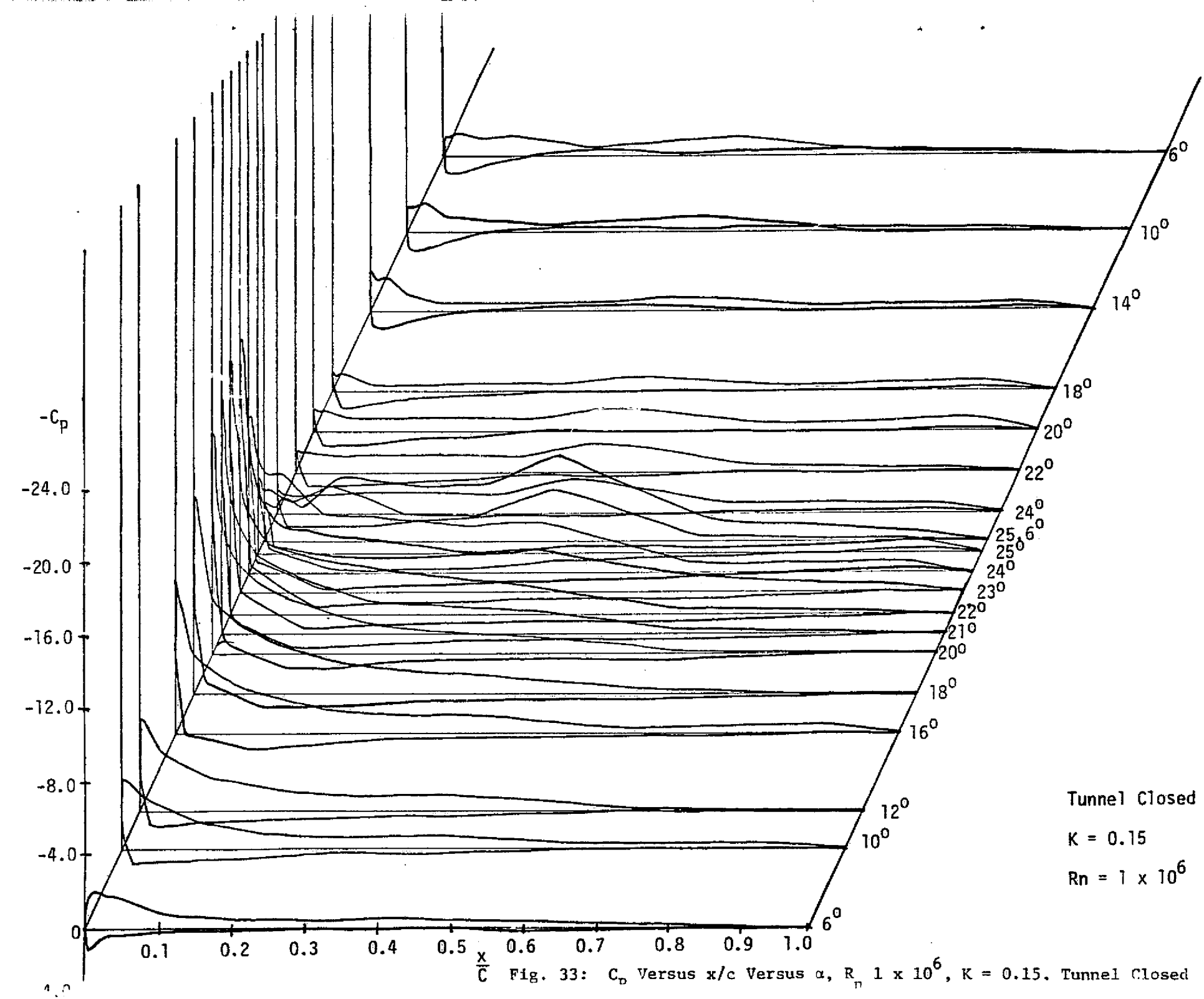

Fig. 33: C_p Versus x/c Versus α, R_n 1 x 10^6, K = 0.15. Tunnel Closed

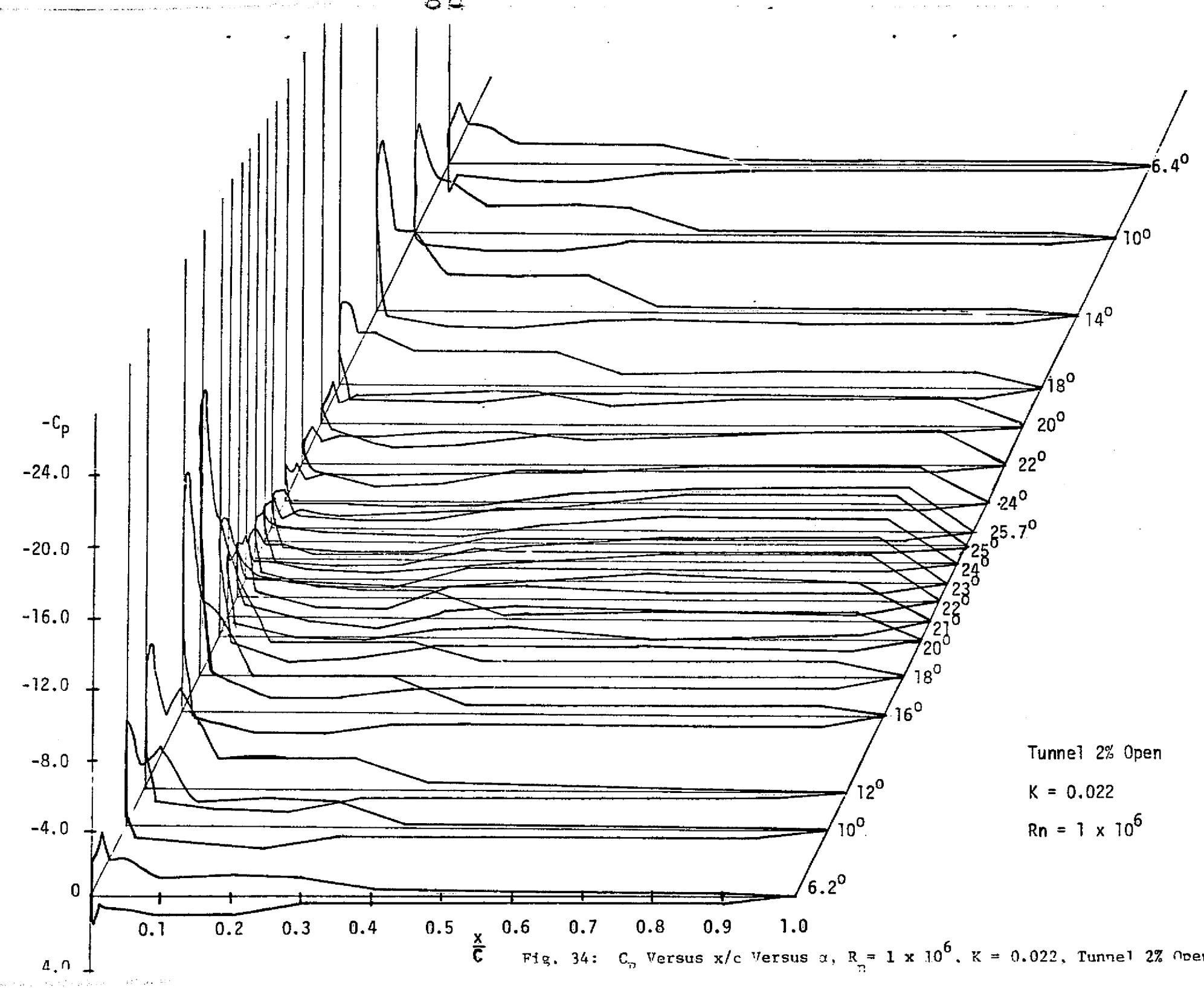

Fig. 34: C_p Versus x/c Versus α, $R_n = 1 \times 10^6$, K = 0.022, Tunnel 2% Open

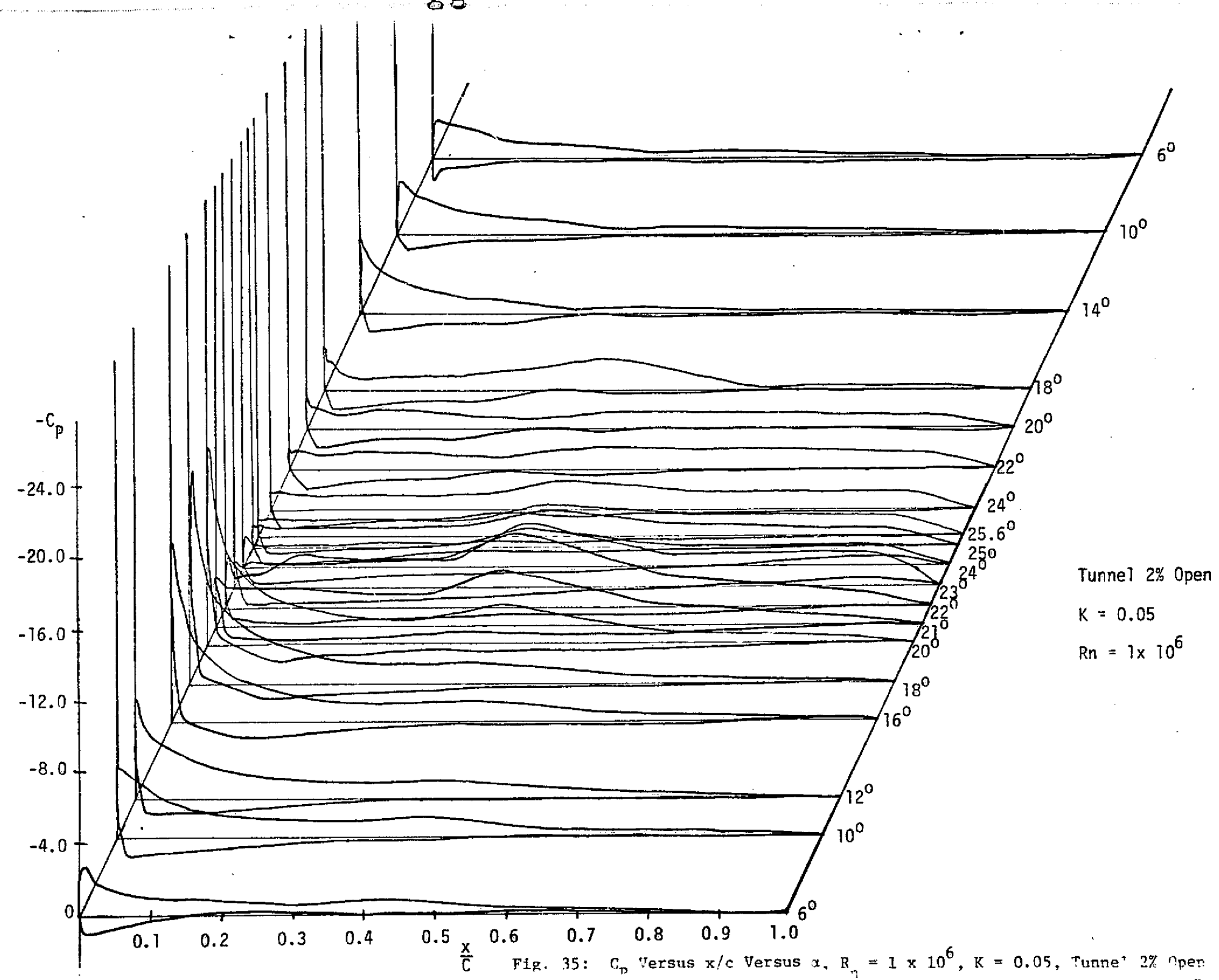

Fig. 35: C_p Versus x/c Versus α, $R_n = 1 \times 10^6$, K = 0.05, Tunnel 2% Open

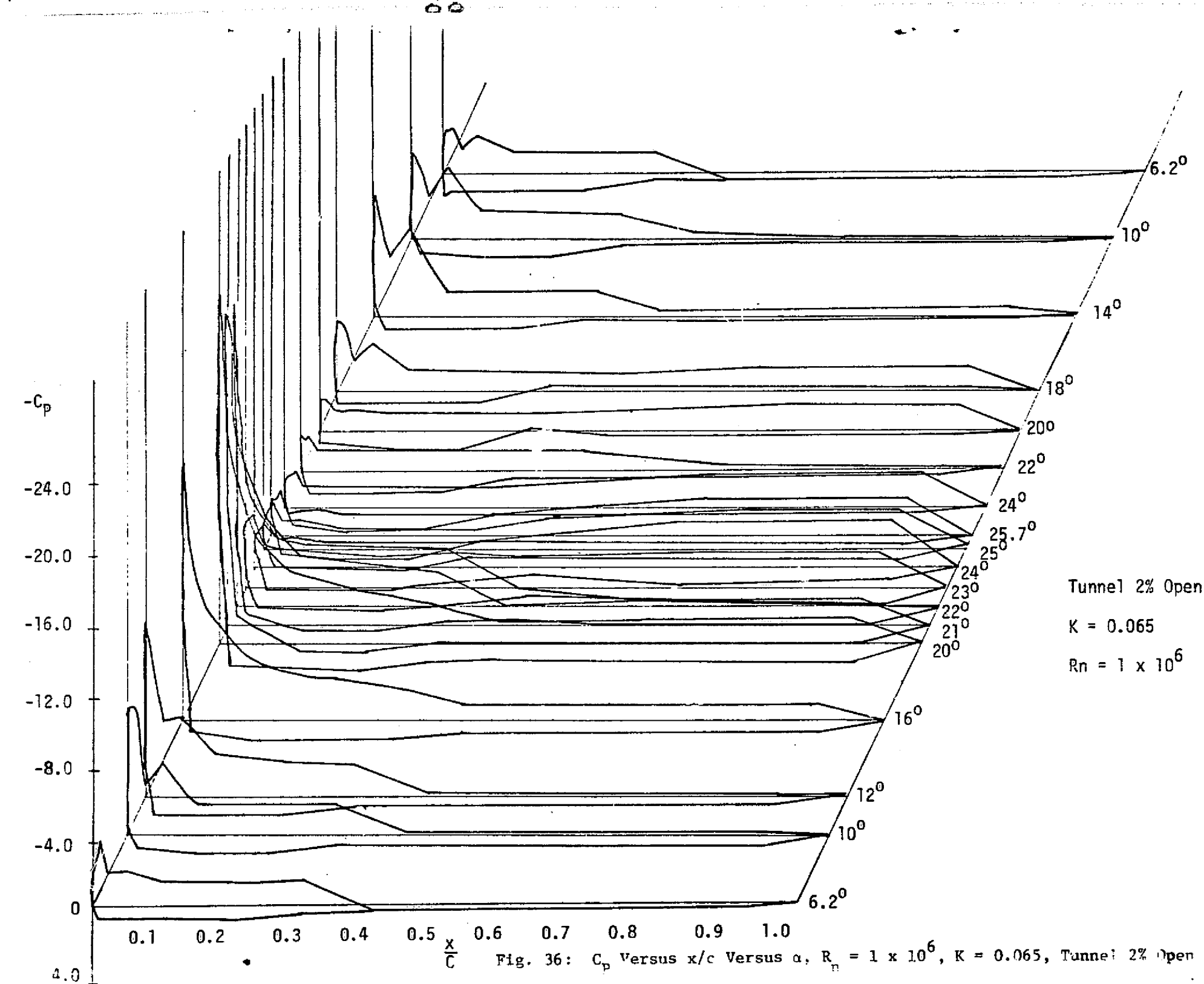

Fig. 36: C_p Versus x/c Versus α, $R_n = 1 \times 10^6$, K = 0.065, Tunnel 2% Open

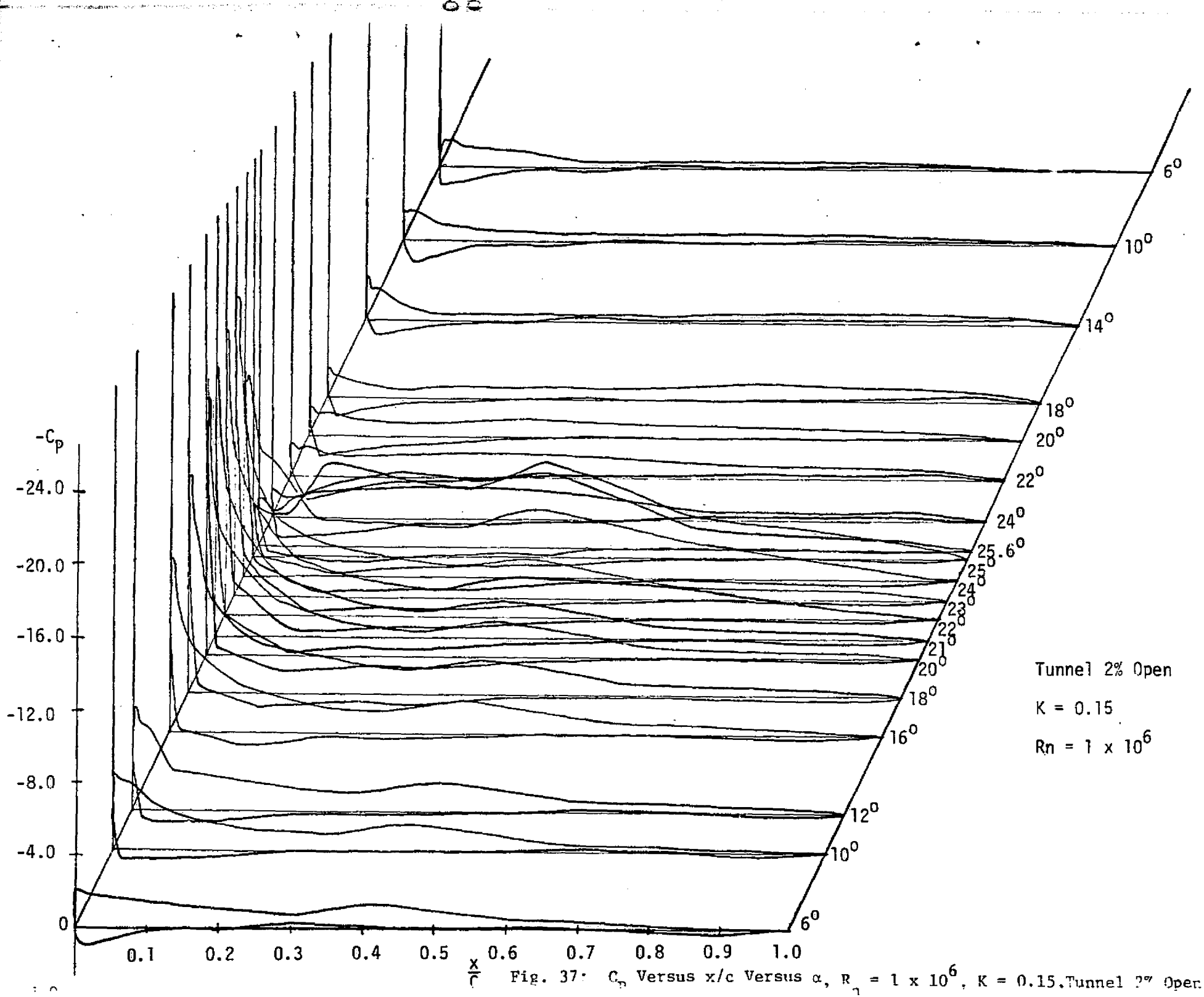

Fig. 37· C_p Versus x/c Versus α, R_n = 1 x 10^6, K = 0.15, Tunnel 2% Open

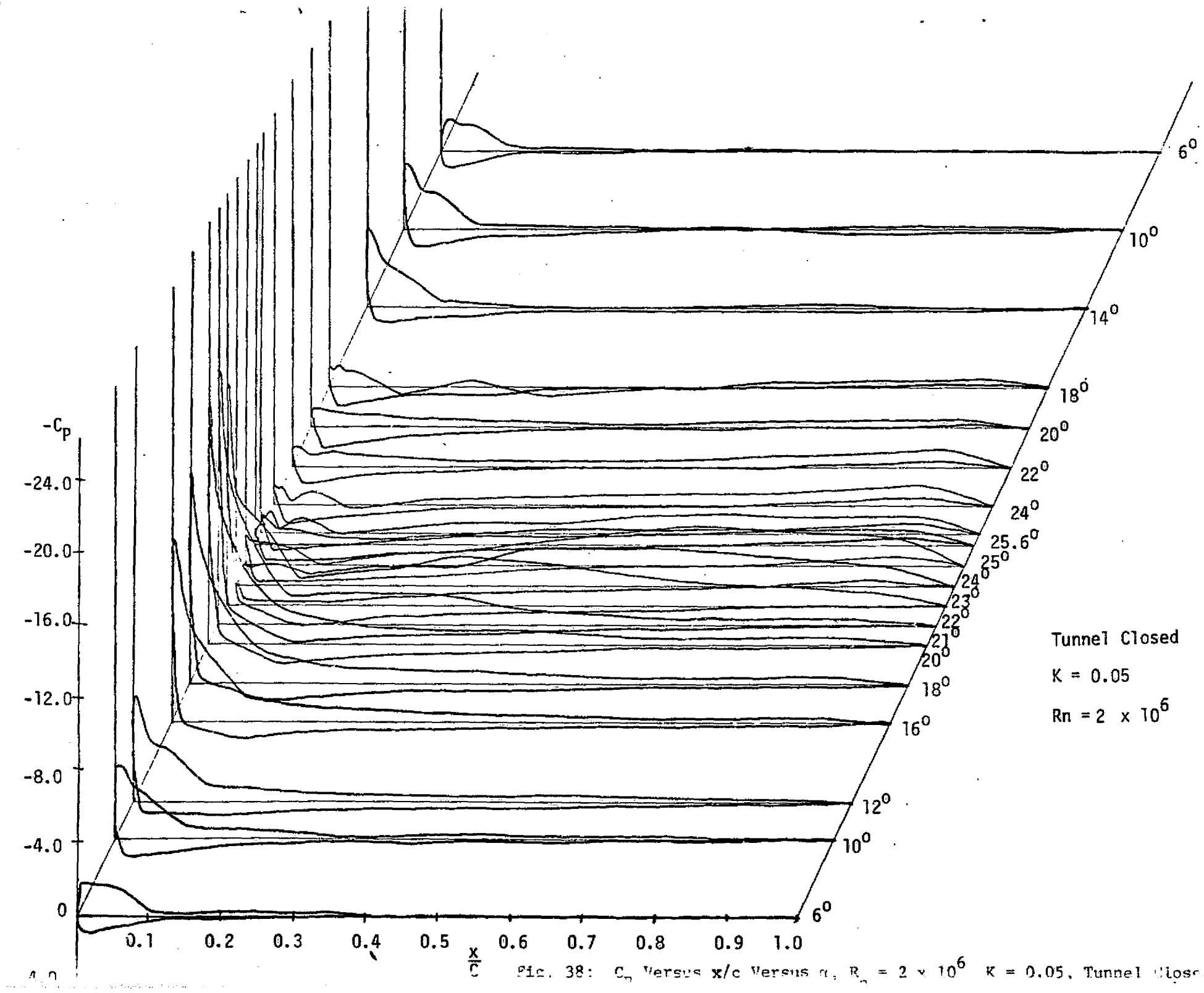

Fig. 38: C_p Versus x/c Versus α, $R_n = 2 \times 10^6$ K = 0.05, Tunnel Closed

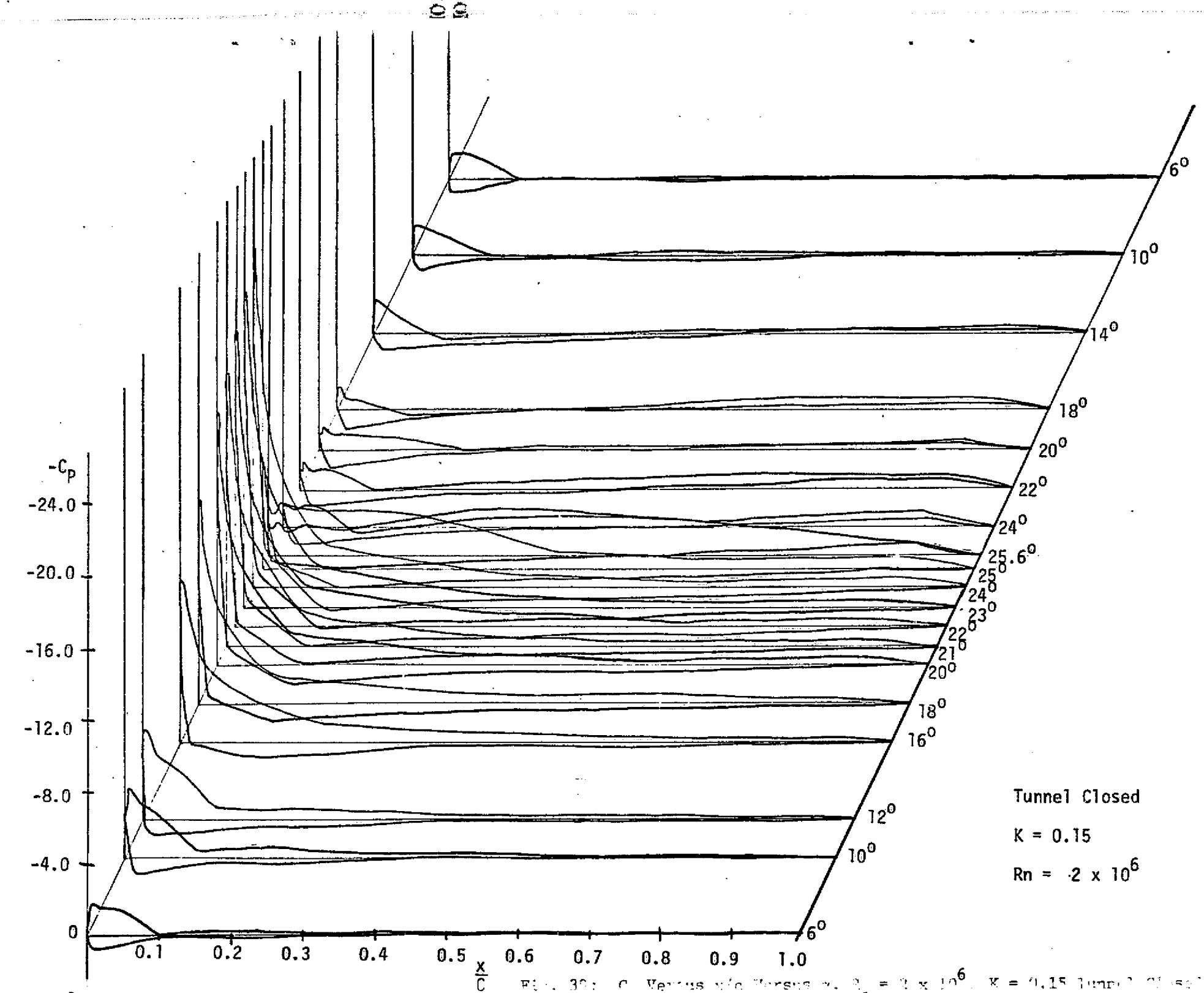

Fig. 30: C_p Versus x/c Versus α, $R_n = 2 \times 10^6$, K = 0.15 Tunnel Closed

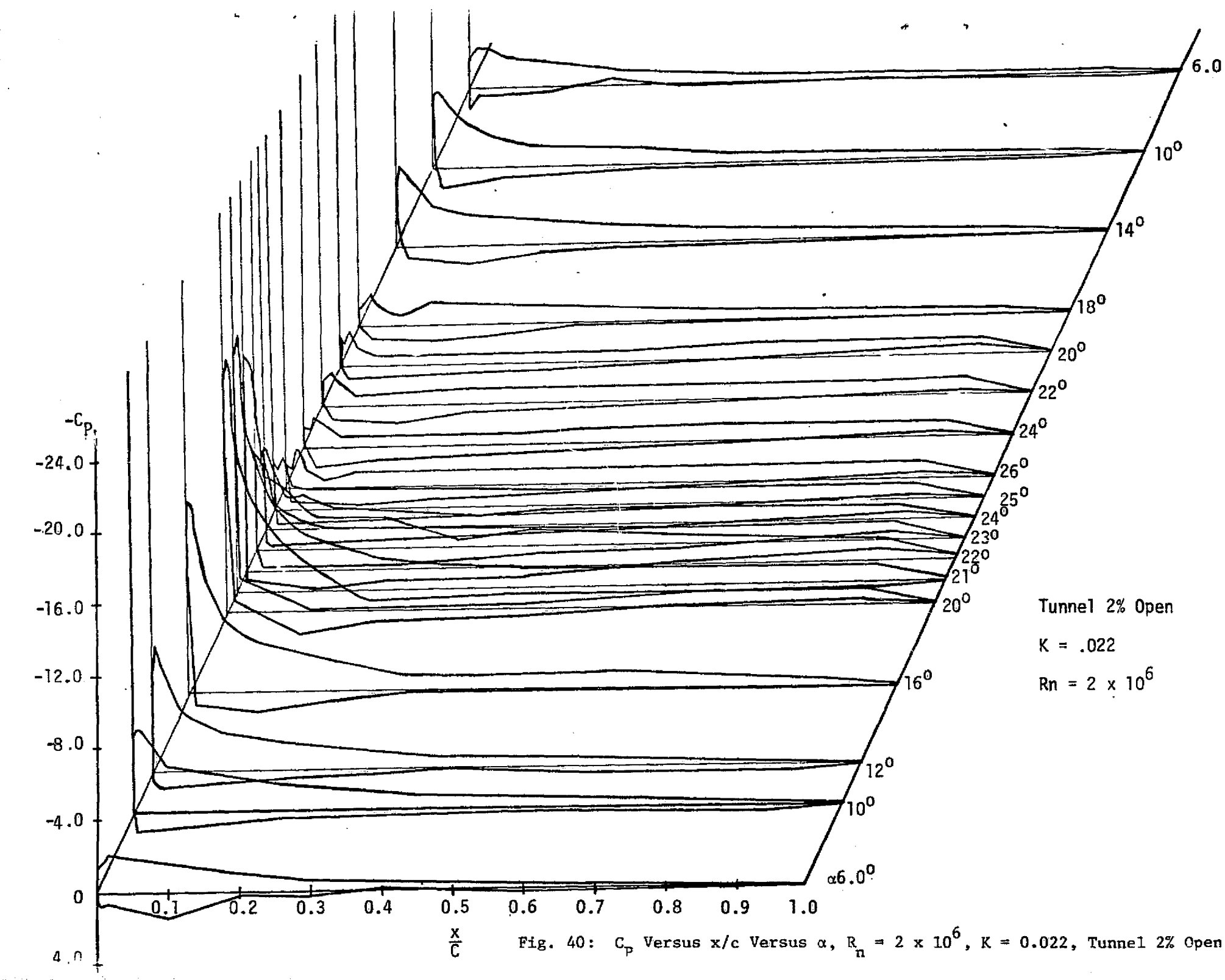

Fig. 40: C_p Versus x/c Versus α, R_n = 2 x 10^6, K = 0.022, Tunnel 2% Open

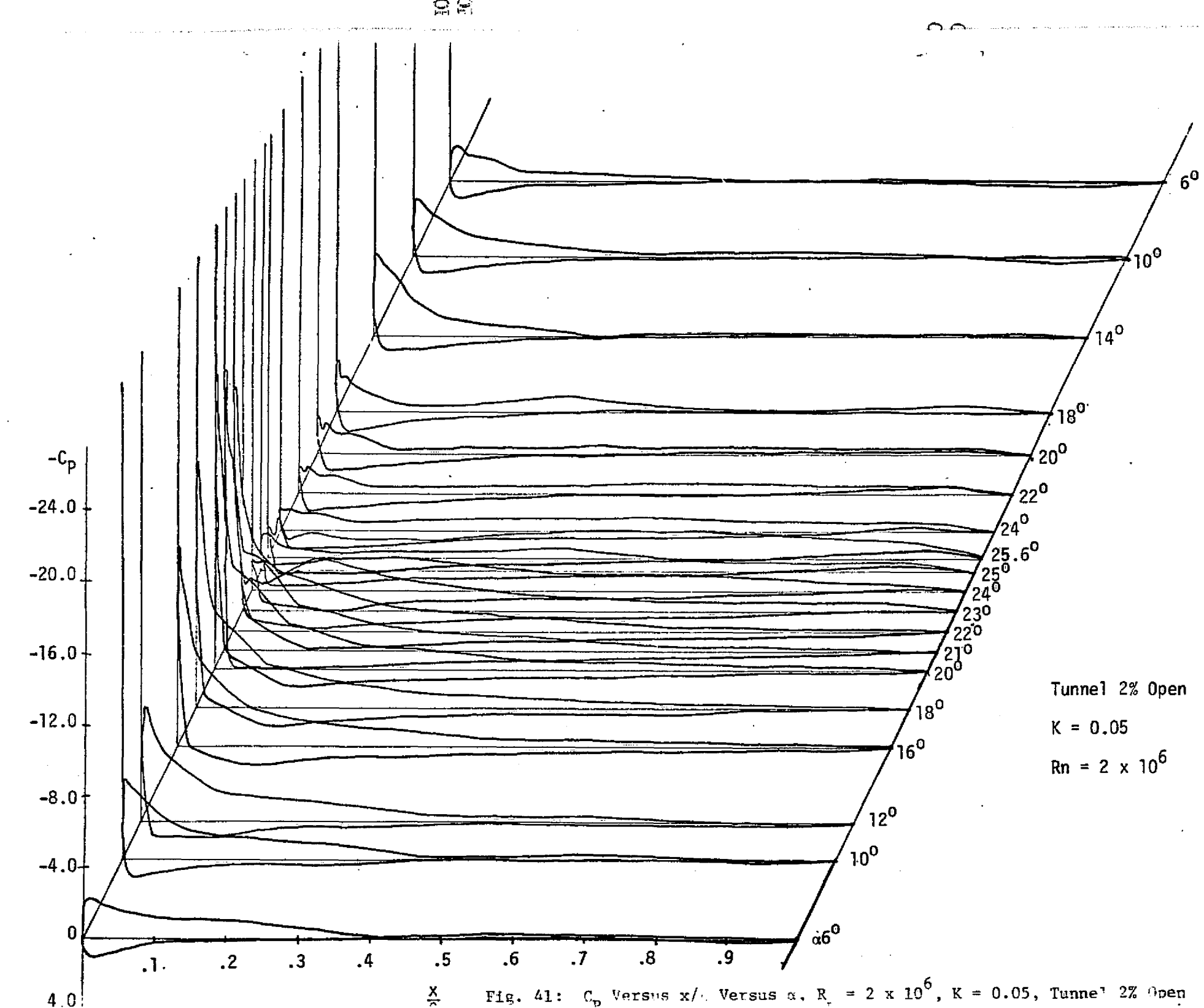

Fig. 41: C_p Versus x/c Versus α, R_c = 2 x 10^6, K = 0.05, Tunnel 2% Open

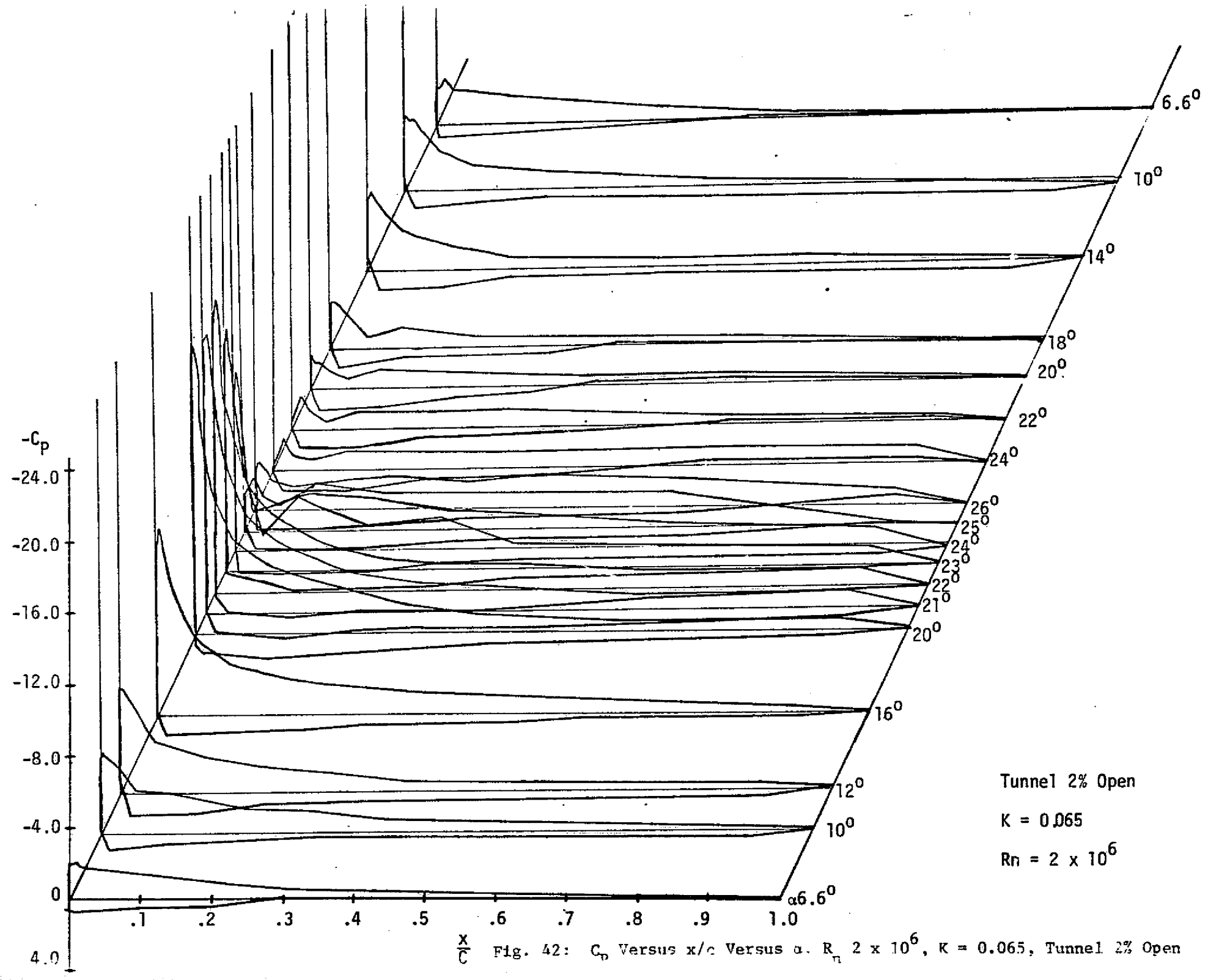

Fig. 42: C_p Versus x/c Versus α. R_n 2 x 10^6, K = 0.065, Tunnel 2% Open

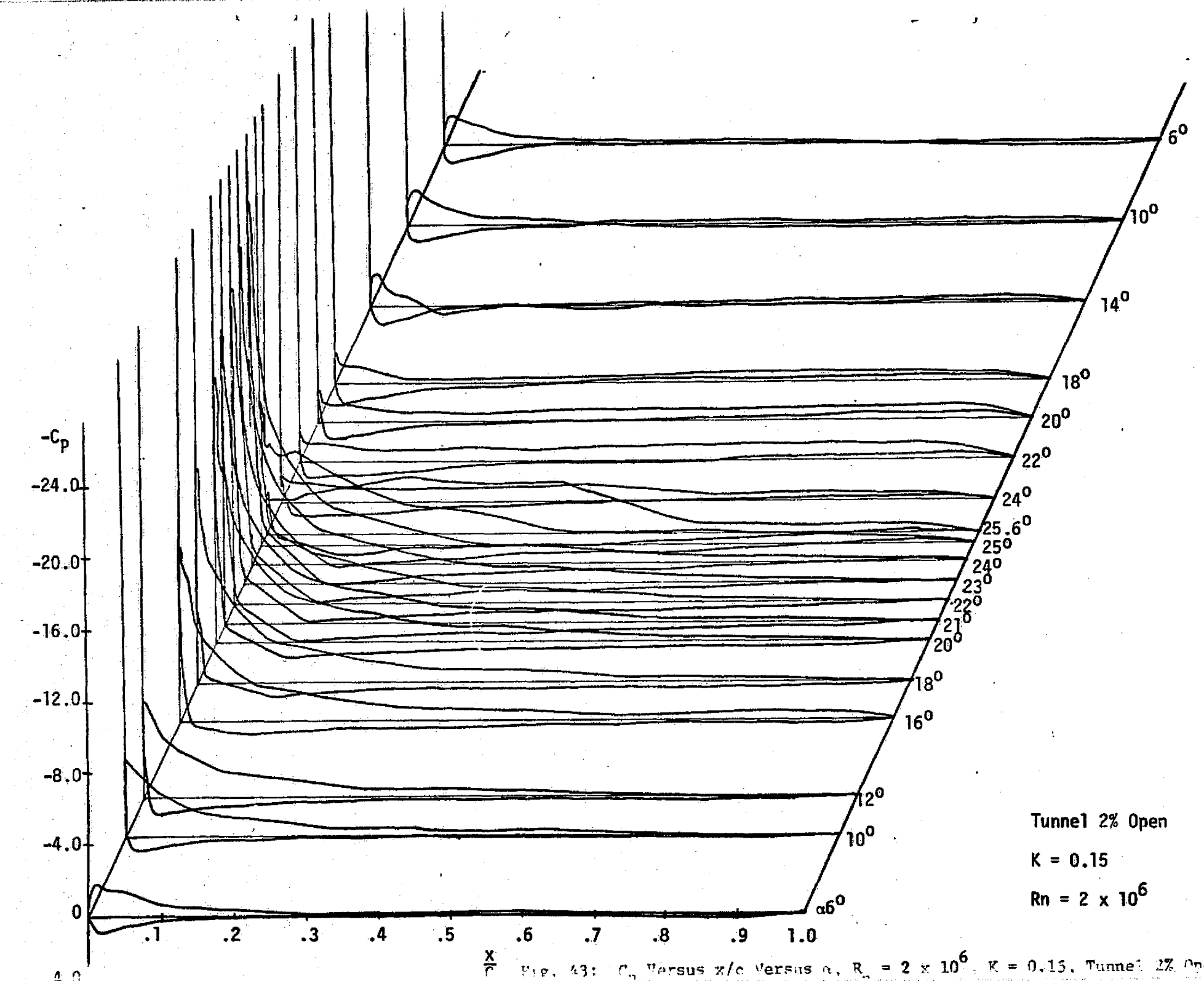

Fig. 43: C_p Versus x/c Versus α, R_n = 2 x 10^6, K = 0.15, Tunnel 2% Open

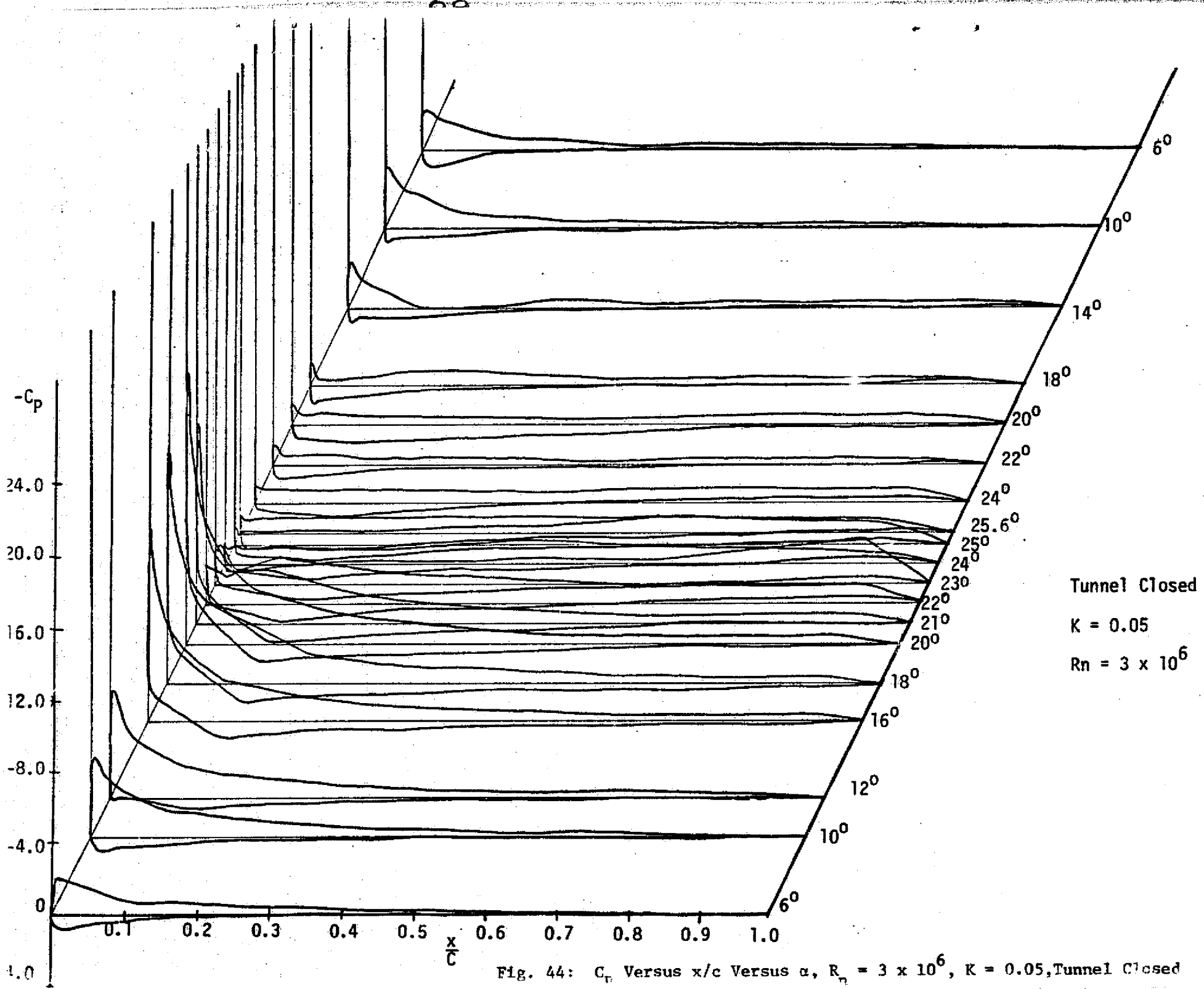

Fig. 44: C_p Versus x/c Versus α, $R_n = 3 \times 10^6$, K = 0.05, Tunnel Closed

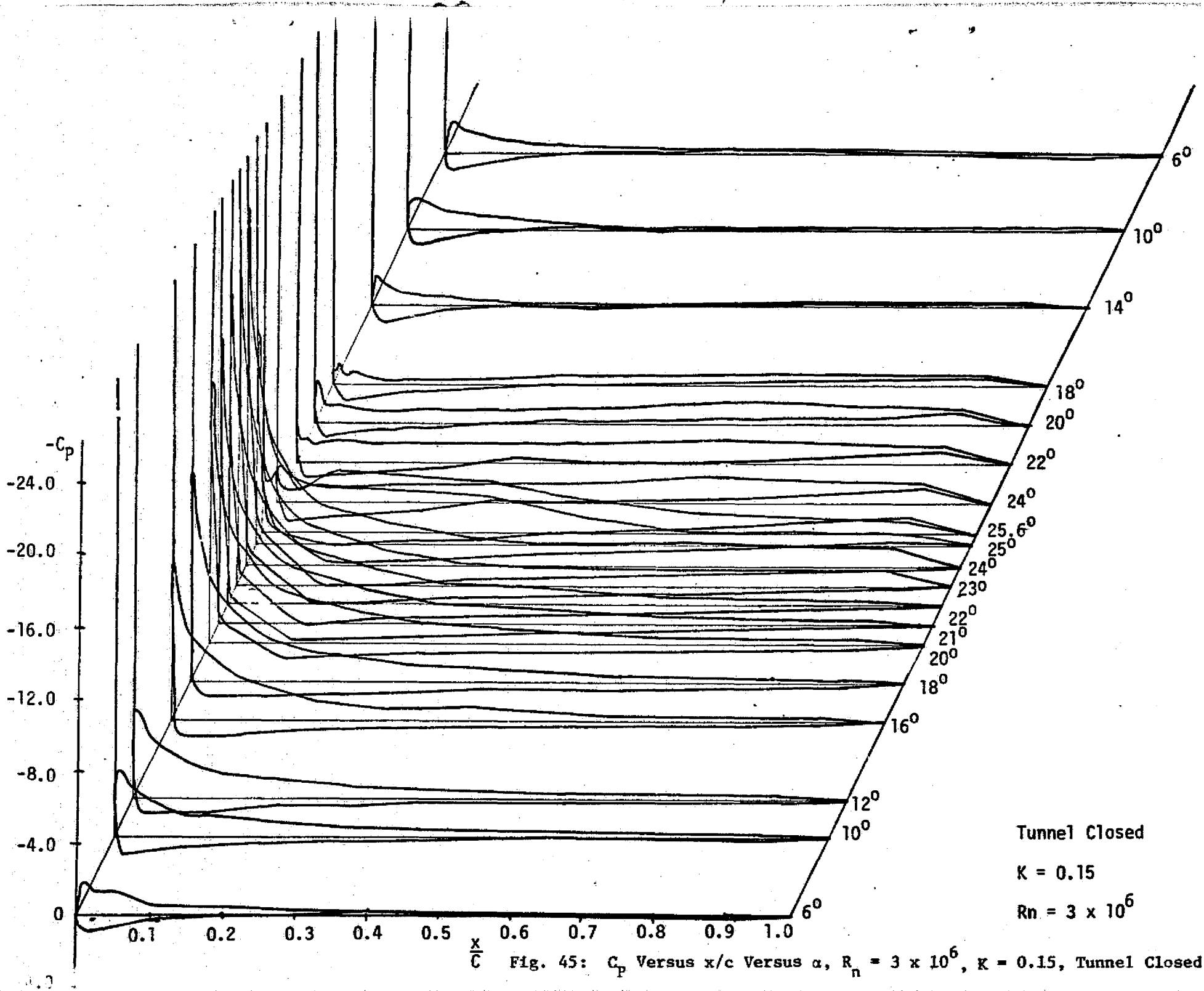

Fig. 45: C_p Versus x/c Versus α, $R_n = 3 \times 10^6$, K = 0.15, Tunnel Closed

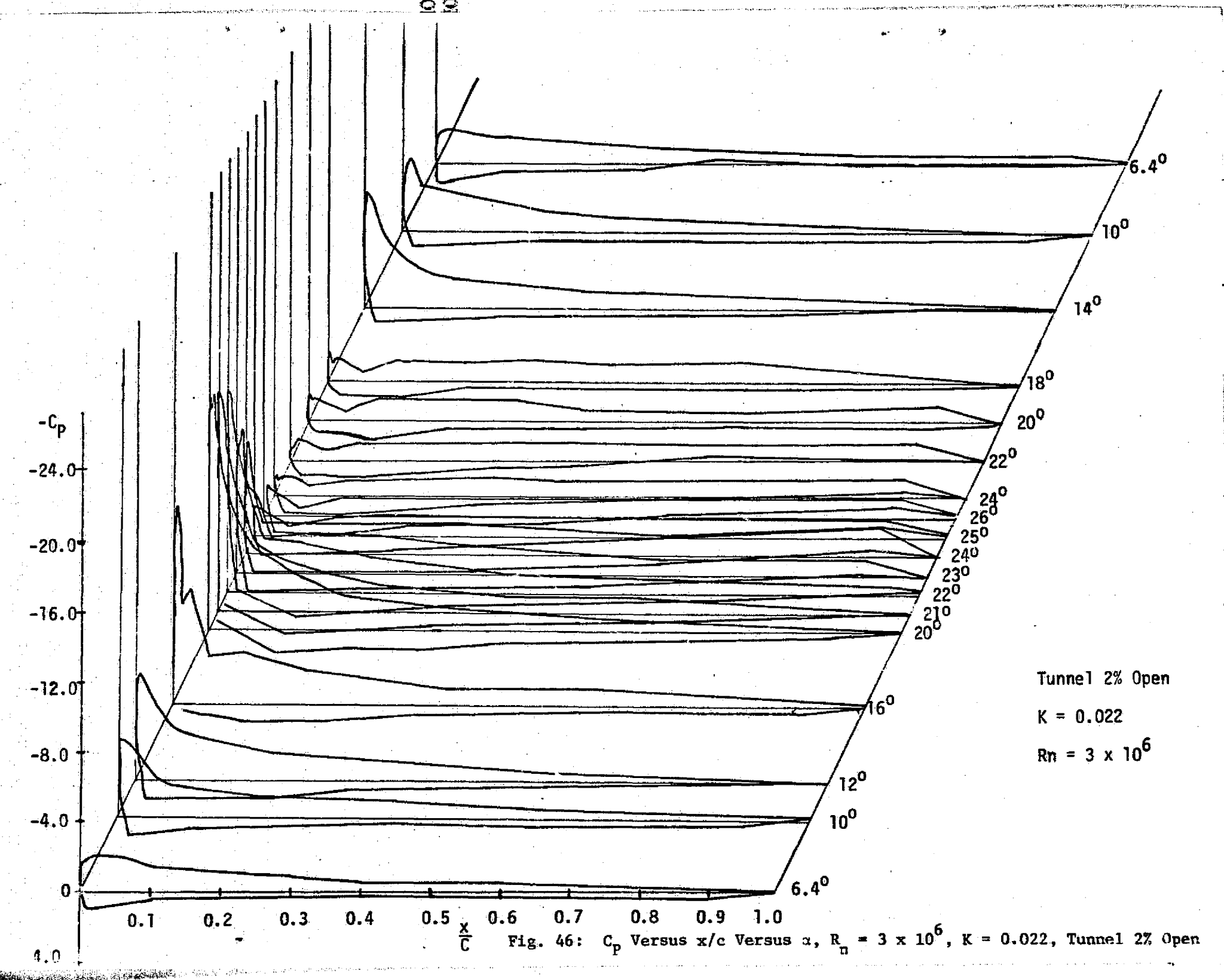

Fig. 46: C_p Versus x/c Versus α, R_n = 3 x 10^6, K = 0.022, Tunnel 2% Open

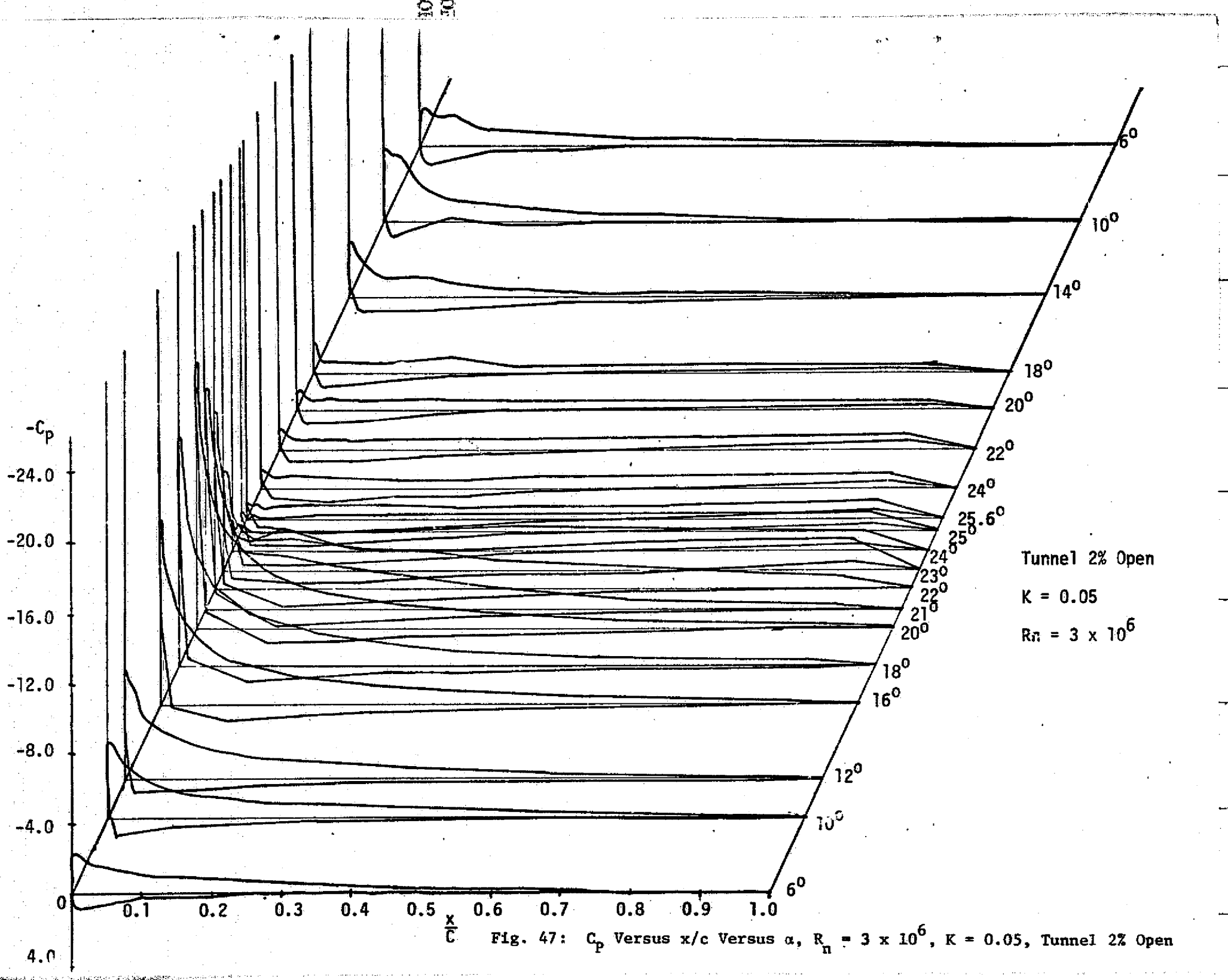

Fig. 47: C_p Versus x/c Versus α, R_n = 3 x 10^6, K = 0.05, Tunnel 2% Open

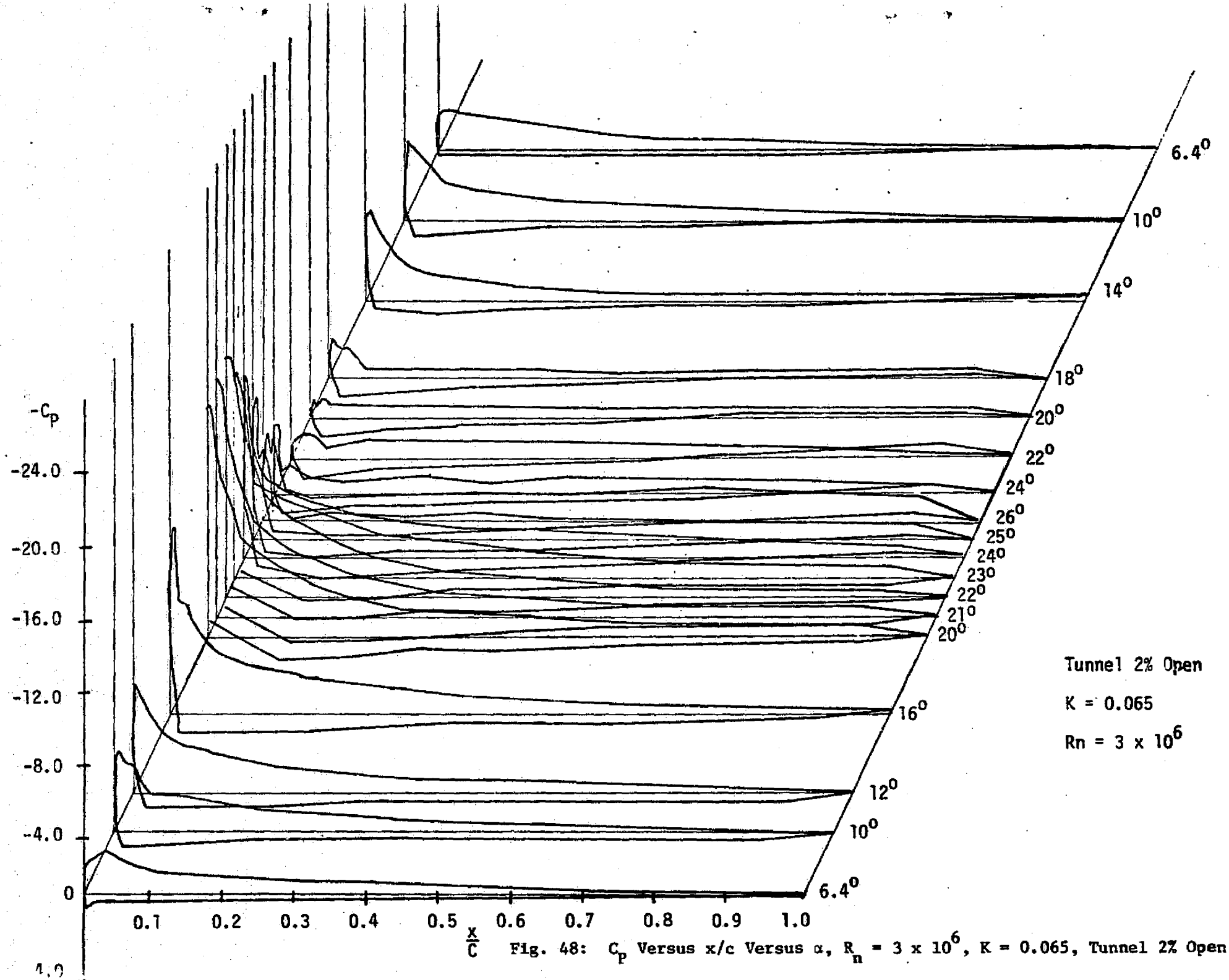

Fig. 48: C_p Versus x/c Versus α, $R_n = 3 \times 10^6$, K = 0.065, Tunnel 2% Open

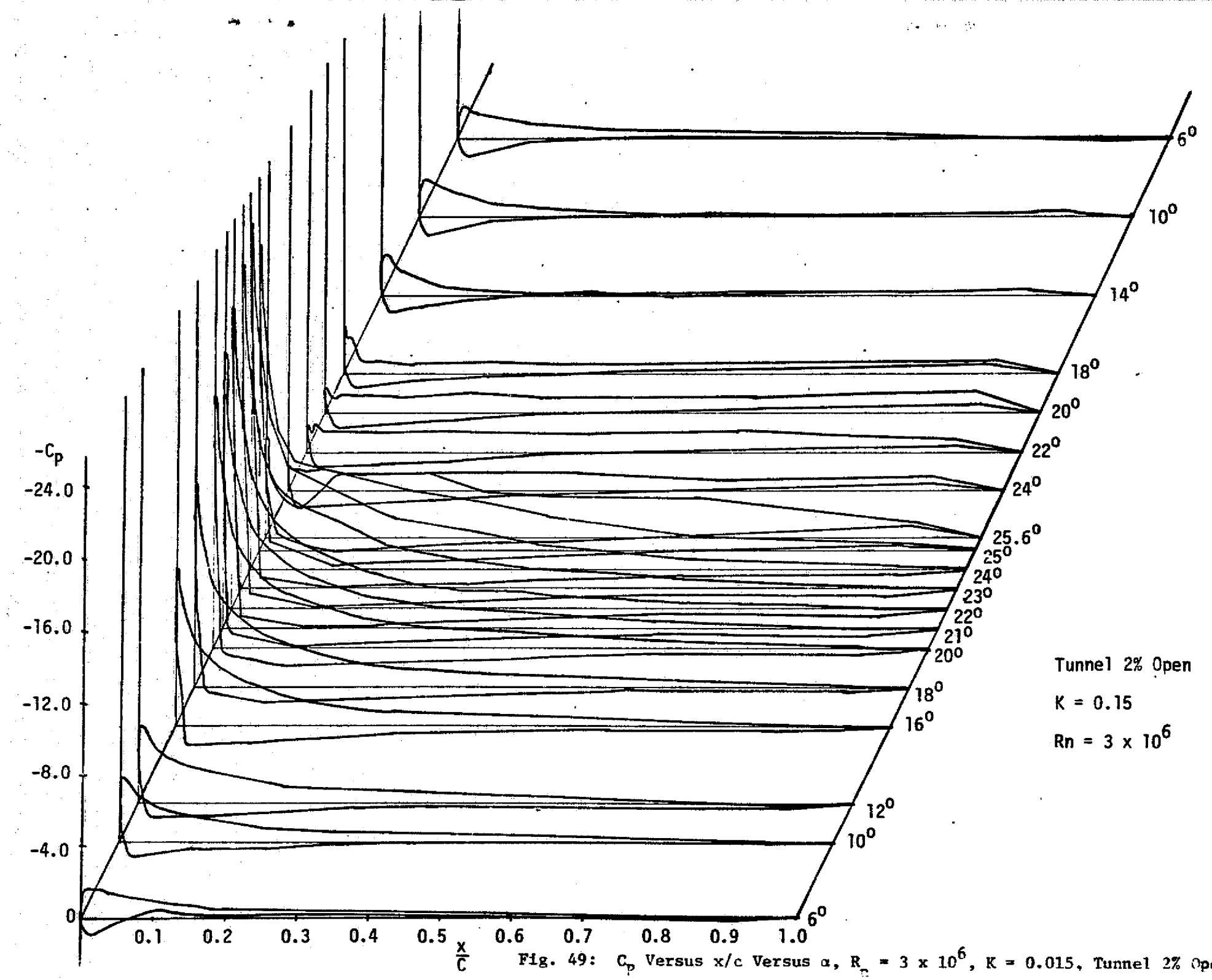

Fig. 49: C_p Versus x/c Versus α, R_n = 3 x 10^6, K = 0.015, Tunnel 2% Open